"Alexandru Ioan Cuza" University of IASI

FACULTY OF CHEMISTRY

DOCTORAL SCHOOL OF CHEMISTRY

MAGNETIC NANOPARTICLES WITH DIFFERENT APPLICATIONS

PhD THESIS SUMMARY

PhD supervisor:

Univ. Prof. Dr. Aurel PUI

PhD student:

Chem. Raluca-Ștefania DĂNILĂ

IASI

2024

Content

The abstract contains a brief presentation of the results obtained in the part of personal contributions, general conclusions and a selection of bibliographical references. The table of contents, chapters, figures, equations and tables keep the same numbering as in the content of the PhD thesis.

INTRODUCTION

Current research trends in chemistry are to discover new compounds, including magnetic nanoparticles and nanocomposites, whose properties can be tailored to the targeted fields. Applications in which these compounds can be used include: removal of dyes from contaminated water using magnetic nanoparticle sorbents, determination of enzyme activity following interaction with magnetic nanocomposites, adsorption and release of drugs on magnetic nanoparticle sorbents.

Based on these premises, the aim of this PhD thesis is to synthesize, characterize and study the applications of a series of nanocomposites, consisting of ferrite-type magnetic nanoparticles embedded in a hydroxyapatite matrix. The advantages obtained from this synthesis consisted in the improvement of biocompatibility and the increase of the value for specific surface area.

Structurally, the thesis consists of two parts: literature review (Part I) and personal contributions (Part II). In the first part, literature data reported on the synthesis methods to date, characterization, and applications of magnetic nanoparticles were described. The second part comprises the detailed presentation of personal contributions, which were based on the fulfillment of certain objectives, namely (1) synthesis of MFe_2O_4 (M= Co, Cu, Mg, Mn, Ni) ferrite-type magnetic nanoparticles and nanocomposites based on ferrite and hydroxyapatite (HaP); (2) synthesis of mixed ferrite types $Co_{1-x}Zn_xFe_2O_4$, $Co_{1-x}Zn_xFe_2O_4$@Ag, $Mn_{1-x}Zn_xFe_2O_4$, $Mn_{1-x}Zn_xFe_2O_4$@Ag (x = 0.5-0.1); (3) characterization of the samples synthesized by different techniques and the study of some applications for the obtained nanocomposites.

The novel elements brought to the field of research by this PhD thesis refer to the study of two applications of the synthesized materials: adsorption of Congo red dye on a $CoFe_2O_4$@HaP sorbent and determination of the enzymatic activity of α-glucosidase following interaction with the nanocomposite $MgFe_2O_4$@HaP@APTES. The results of these applications have been published in two scientific articles in Web of Science journals with impact factor (Materials Today Communication - Elsevier, Materials - MDPI).

PART 2. Personal Contributions

Purpose and objectives

The aim of the PhD thesis is the synthesis of ferrite-based nanocomposites with various applications.

Objectives

The possibility of applying nanoparticles in several scientific fields is one of the premises of the proposal for the present research topic. In the elaboration of the PhD thesis the following objectives were considered:

1. *Synthesis of magnetic nanoparticles of the ferrite type MFe_2O_4, where M = Co, Cu, Mg, Mn, Ni;*
2. *Synthesis of nanocomposites composed of ferrites and hydroxyapatite (HaP) of the type MFe_2O_4@HaP, where M = Co, Cu, Mg, Mn, Ni;*
3. *Synthesis of mixed ferrites of the type $Co_{1-x}Zn_xFe_2O_4$, $Co_{1-x}Zn_xFe_2O_4$@Ag and $Mn_{1-x}Zn_xFe_2O_4$, $Mn_{1-x}Zn_xFe_2O_4$@Ag (x = 0.5-0.1);*
4. *Characterization of nanocomposites by various techniques;*
5. *The study of some applications of the obtained nanocomposites such as:*
    - *Removal of Congo red dye from aqueous solutions by adsorption on a $CoFe_2O_4$@HaP nanocomposite;*
    - *Encapsulation efficiency of ibuprofen on a series of adsorbents based on ferrites and nanocomposites;*
    - *Testing the enzyme activity of α-glucosidase following the interaction with the $MgFe_2O_4$@HaP nanocomposite.*

III. Synthesis and characterization of nanocomposites based on ferrite nanoparticles and hydroxyapatite (HaP)

III.1. Synthesis of ferrites and nanocomposites

III.1.1. Synthesis of ferrite nanoparticles of the MFe_2O_4 type, where M= Co, Cu, Mg, Mn, Ni

The ferrite samples used in the experimental studies of the doctoral thesis were synthesized by the co-precipitation method in aqueous solution adapted from the literature references [125, 126]. Thus, a solution of $MCl_2 \cdot 6H_2O$ 0.2 M was mixed with a solution of $FeCl_2 \cdot 6H_2O$ 0,4 M under continuous magnetic stirring at a temperature of 353.15K. To prevent particle agglomeration, a 1% carboxymethylcellulose (CMC) solution was added as a surfactant. The precipitation of the oxides was achieved by adding a 3 M NaOH solution. The pH was checked and adjusted to reach a value between 11-12. The black precipitate obtained was washed with distilled water to remove NaCl resulting from the synthesis process, dried in an oven for 24 hours at 343.15K, then calcined for 6 hours at 773.15K in a calcination furnace.

III.1.2. Synthesis of MFe_2O_4@HaP type nanocomposites

The ferrite nanoparticles are dispersed in 25 mL of ethanol, together with 0.1 g of hexadecyltrimethylammonium bromide (CTAB - surfactant) and 25 mL of 0.3 M H_3PO_4 under continuous mechanical stirring at 333.15K, and the solution pH of 10.5 is maintained with NH_4OH. Then, a 0.5 M $Ca(NO_3)_2$ solution is added dropwise over the formed solution and allowed to mature overnight. The particles are washed with distilled water until the pH is neutral, by decantation, dried in an oven for 24 hours at 343.15K, and then calcined for 4 hours at 773.15K in a calcination furnace. The working protocol used is adapted from that proposed in the bibliographic references [127, 128].

III.2. Characterization methods

III.2.1. X-ray diffraction (XRD) analysis

The purity of the synthesized samples was confirmed by X-ray diffraction (XRD). The XRD diffractograms obtained for the samples analyzed are shown in Figures 16 and 17.

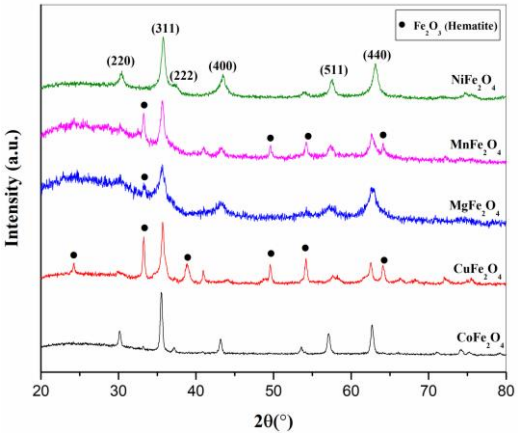

Figure 16. X-ray diffractograms for synthesized samples

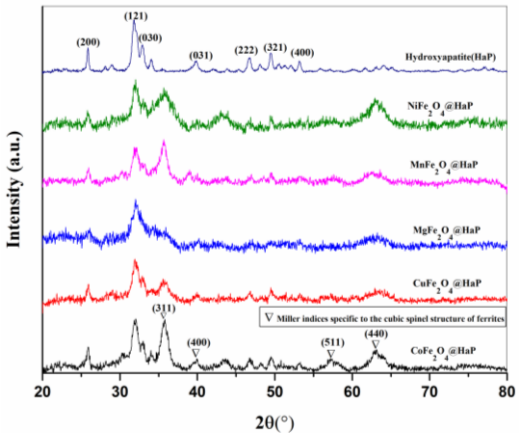

Figure 17. X-ray diffractograms for the synthesized nanocomposites

After analyzing the diffractograms in Figures 16 and 17, the following aspects were observed: all samples show the phase corresponding to the cubic spinel structure, space group *Fd-3m*, phase identified from ICSD databases; the secondary phase characteristic of the hexagonal structure of hematite was also observed by correlation with the database ICSD [98-009-5862]; the structure of hydroxyapatite was confirmed by the presence of the phase with hexagonal structure and space group *P63/m* ICSD [98-009-4268]. For the analyzed samples, the crystallite sizes were also determined (tables 4 and 5) using the Scherrer equation [132]:

$$D = \frac{K \times \lambda}{B \times cos\theta_B} \quad (2)$$

Where: D = crystallite size;

K = constant dependent on the shape of the crystallite (0.89);

B = FWHM (Full Width at Half Maximum – The width of the diffraction maxima measured at half its maximum amplitude);

θ_B= Bragg angle, diffraction angle;

λ = X-ray wavelength (nm).

Table 4. Crystallite sizes corresponding to simple ferrites and hydroxyapatite

No.	Sample	Crystallite size (nm)
1	$CoFe_2O_4$	44.46
2	$CuFe_2O_4$	31.00
3	$MgFe_2O_4$	30.78
4	$MnFe_2O_4$	22,26
5	$NiFe_2O_4$	35.79
6	Hydroxyapatite (HaP)	38.19

Table 5. Crystallite sizes corresponding to nanocomposites

Sample	Crystallite Sizes (nm)		
	Spinel	HaP	Nanocomposite
$CoFe_2O_4$@HaP	66.78	48.99	57.88
$CuFe_2O_4$@HaP	58.04	20.95	39.49
$MgFe_2O_4$@HaP	58.47	12.94	35.70
$MnFe_2O_4$@HaP	30.60	16.84	23.72
$NiFe_2O_4$@HaP	55.43	17.15	36.29

In order to calculate by means of the Scherrer equation the values of the crystallite sizes of the synthesized samples, the main diffraction maxima identified from the processing of the diffractograms were taken into account. Table 4 shows the average values of the crystallite size obtained for the analyzed ferrites. For nanocomposites, the crystallite sizes were calculated from the average of the values obtained for spinel and hydroxyapatite (Table 5).

III.2.2. Analysis by FT-IR spectroscopy

In order to observe whether the specific links of the structure of ferrites and nanocomposites formed by ferrites and hydroxyapatites can be found in the synthesized samples, their analysis was carried out by FT-IR spectroscopy. The spectra obtained were shown in Figures 18-20.

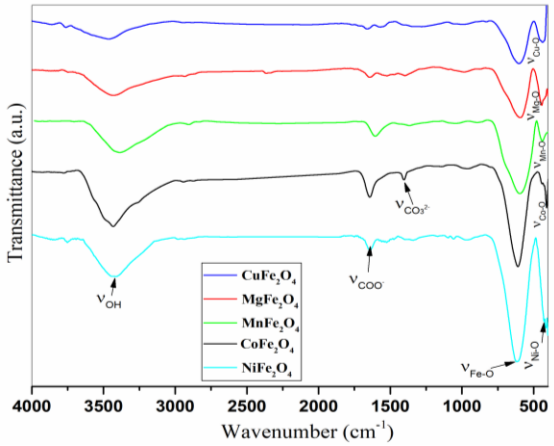

Figure 18. FT-IR spectra of simple

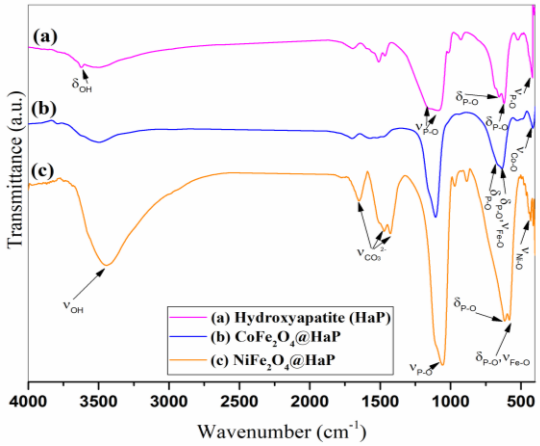

Figure 19. FT-IR spectra ferrite samples for samples of (a) hydroxyapatite (HaP); (b) $CoFe_2O_4$@HaP; (c) $NiFe_2O_4$@HaP

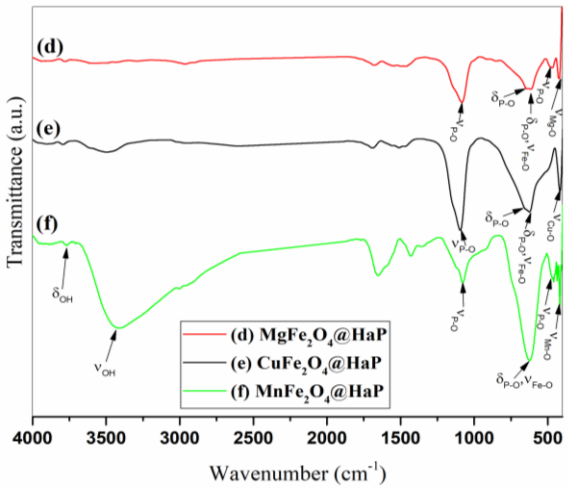

Figure 20. FT-IR spectra for the samples of (d) $MgFe_2O_4$@HaP; (e) $CuFe_2O_4$@HaP; (f) $MnFe_2O_4$@HaP

In the FT-IR spectra of figure 18, of the simple ferrite samples, the corresponding M-O bonds were found following the identification of the absorption bands in the range 602-413 cm^{-1}. From the spectra in figure 19 (a), the absorption bands specific to hydroxyapatite were observed in the domains 1020-1100 cm^{-1} and 565-610 cm^{-1}. These bands are also found in the spectra of the nanocomposites (Fig. 19 b,c and Fig. 20 d,f), which indicates their successful acquisition.

III.2.3. Analysis of morphology and composition by SEM and EDX

Morphology of cobalt ferrite sample and $CoFe_2O_4$@HaP nanocomposite was investigated by scanning electron microscopy (SEM). The results obtained can be seen in figures 21 - 22 and show the formation of agglomerates with irregular shapes.

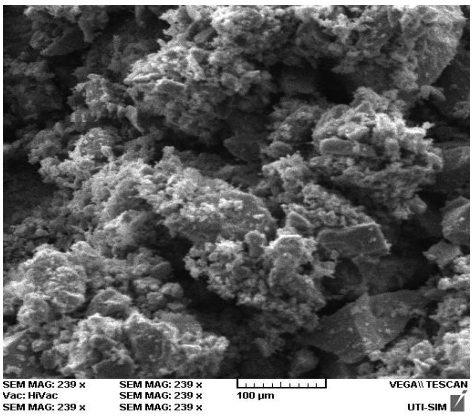

Figure 21. SEM image for the sample of $CoFe_2O_4$

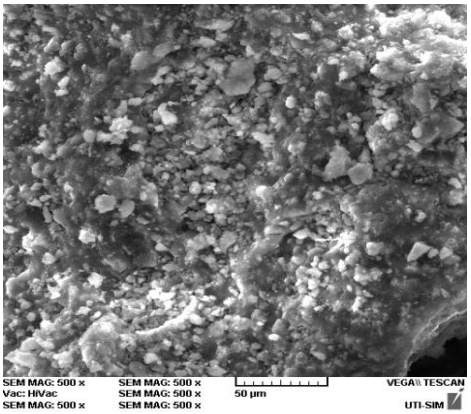

Figure 22. SEM image for the sample of $CoFe_2O_4$@HaP

Elemental composition of $CoFe_2O_4$ and $CoFe_2O_4$@HaP samples were analyzed by EDX technique. The images in figures 23 - 24 indicate the presence of elements specific to both samples without other impurities, which have an uneven distribution.

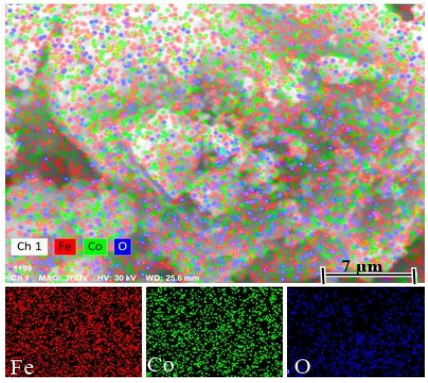

Figure 23. Composition by elements of $CoFe_2O_4$ from EDX

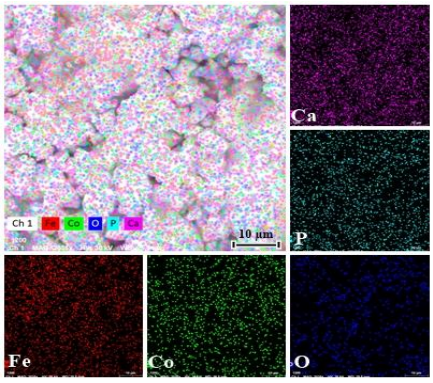

Figure 24. Composition by elements of $CoFe_2O_4$@HaP from EDX

With the help of EDX analysis, it was confirmed that $CoFe_2O_4$ and $CoFe_2O_4$@HaP samples were obtained without impurities by assigning the energy maxima with the elements specific to their composition (Fig. 25).

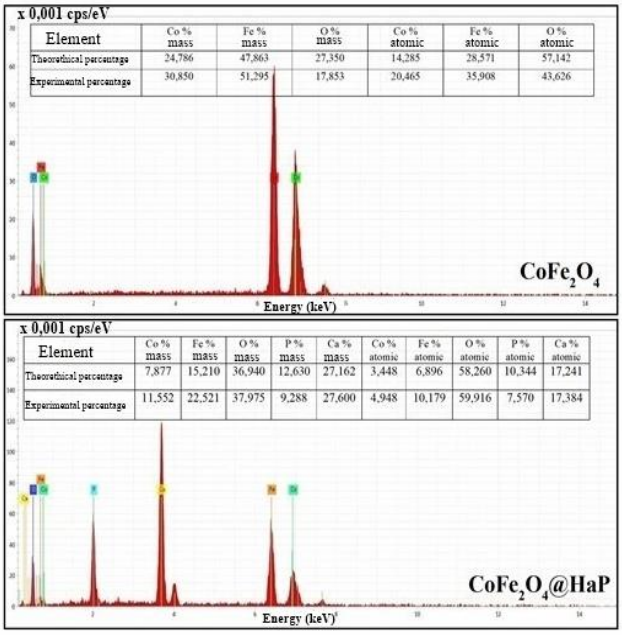

Figure 25. EDX spectrum for the $CoFe_2O_4$ sample and for the $CoFe_2O_4$@HaP sample

Also, the atomic and mass percentages corresponding to the components of the samples were identified theoretically and experimentally, and close values were observed.

III.2.4. Analysis of textural parameters using the BET technique

Characterization of the pore texture of the synthesized materials was performed by analyzing nitrogen adsorption-desorption processes. Figures 25 - 27 show the characteristic isotherms of both simple ferrites and nanocomposites.

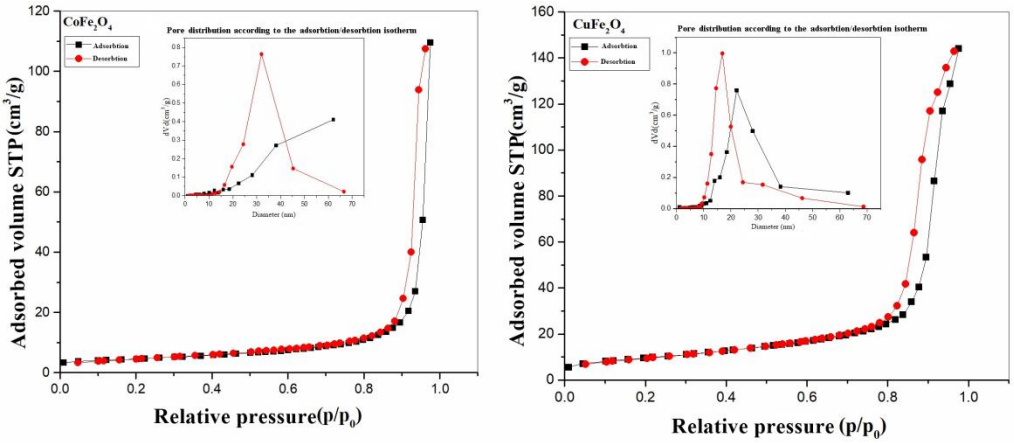

Figure 25. Adsorption-desorption isotherms and pore size distributions for ferrites: $CoFe_2O_4$ and $CuFe_2O_4$

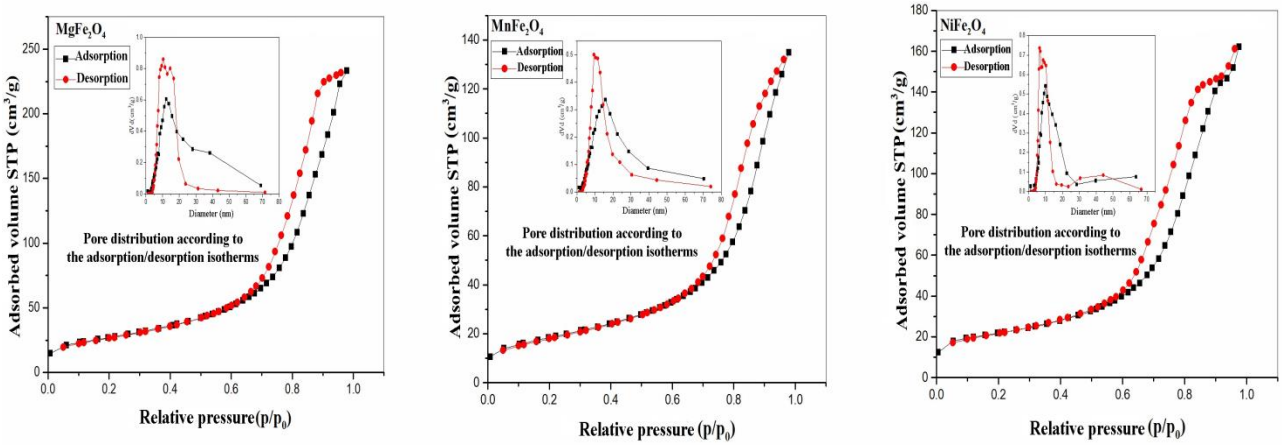

Figure 26. Adsorption-desorption isotherms and pore distributions for ferrites: $MgFe_2O_4$, $MnFe_2O_4$ and $NiFe_2O_4$

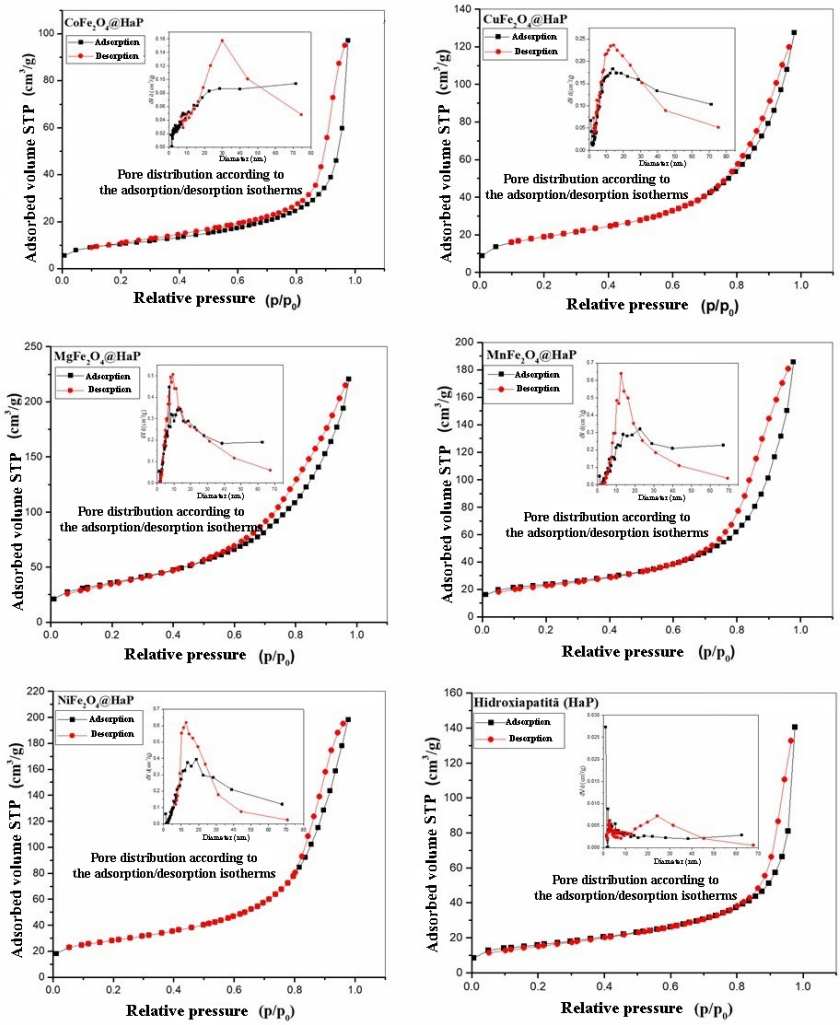

Figure 27. Adsorption-desorption isotherms and pore distributions for the synthesized nanocomposites

For all analyzed samples, the adsorption isothermsshows the appearance of a type IV isotherm according to the IUPAC classification, with a capillary condensation at high relative pressures, characteristic of mesoporous materials. In the case of the analyzed samples, a hysteresis of type H3 is observed, characteristic of slit-type pores. Textural parameters such as specific surface area, average pore size and total pore volume for the synthesized samples were also determined. The highest values of specific surface area and pore volume were attributed to the samples of $MgFe_2O_4$, $NiFe_2O_4$, $MgFe_2O_4$@HaP and $NiFe_2O_4$@HaP. Regarding the diameter of the pores, the values obtained fit them as a size in the field of mesopores, the smallest diameter being found in the case of manganese and nickel ferrites, but also in the case of the $MgFe_2O_4$@HaP type nanocomposite

III.2.5. Analysis of magnetic properties using VSM technique

To identify the magnetic properties of the synthesized samples, they were analyzed using the VSM technique. The hysteresis loops obtained for the analyzed samples are shown in Figures 28 and 29

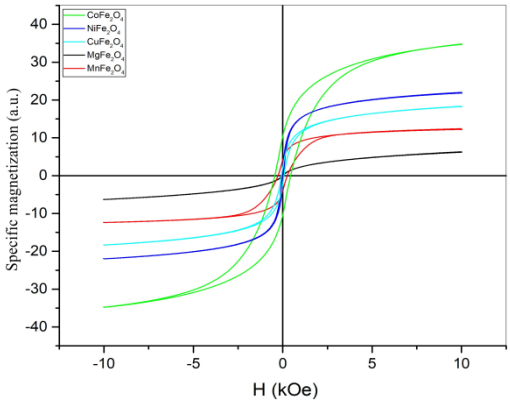

Figure 28. Hysteresis loops of synthesized ferrites

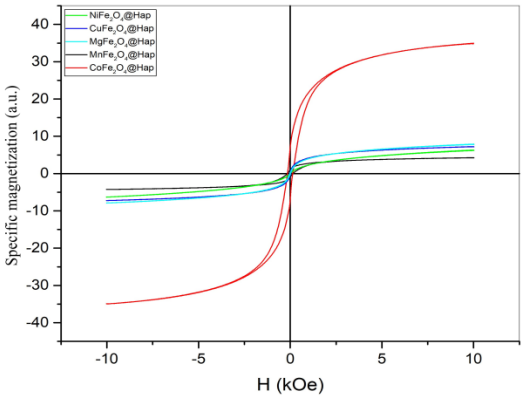

Figure 29. Hysterezis loops of synthesized nanocomposites

Following the interpretation of the hysteresis loops in figures 28 and 29, specific magnetic parameters were determined such as: saturation magnetization (M_s), remanent magnetization (M_r), coercivity (H) and M_s/M_r ratio. The highest values of the magnetizations are for the cobalt ferrite sample (M_r = 40.260 emu/g; M_s = 69.22 emu/g).

III.3. Applications of magnetic heterostructures of the $CoFe_2O_4$@HaP type in wastewater treatment

The aim of the present study is to investigate the potential application of $CoFe_2O_4$@HaP nanocomposite obtained for the removal of Congo red dye from aqueous solutions. Valuable information about the effectiveness of using $CoFe_2O_4$@HaP nanocomposite in wastewater treatment was determined by adsorption studies, by evaluating the adsorption capacity of $CoFe_2O_4$@HaP nanocomposite and by analyzing the kinetic models governing the process.

Adsorption studies were performed using a UV-Vis UV-3100PC spectrophotometer (VWR International Europe bvba, Leuven, Belgium). The absorbance of the supernatant of each sample was measured at 497 nm. The following equation was used to calculate the adsorption capacity:

$$q_e = \frac{(C_i - C_f)V}{m} \quad (3)$$

The terms used in equation (3) are: q_e is the adsorption capacity (mg/g), c_i and c_f are the initial dye concentration and equilibrium dye concentration (mg/L), V is the volume of the dye solution (L) and m is the amount of $CoFe_2O_4$@HaP used (g).

Experimental results

Three experimental factors were investigated during the study: $CoFe_2O_4$@HaP nanocomposite dosage, contact time and temp. The graphs resulting from the experiments are in figure 32(a-j).

For dosing the amount of nanocomposite (Fig. 32 a) a value of 0.49 g/L was chosen and resulted in a dye adsorption capacity of 15.25 mg/g. The optimum adsorption contact time was 50 minutes, with an adsorption capacity value of 15.24 mg/g (Fig. 32 b). The most effective value of dye solution temperature was 319K, the obtained adsorption capacity was 27.97 mg/g (Fig. 32 i).

The experimentally obtained data on the effect of contact time were analyzed using different kinetic models, such as: pseudo first order, pseudo second order (Type 1, Type 2, Type 3 and Type 4) and intra-particle diffusion. The graphs resulting from the experiments are in figure 32(c-h). By plotting q_t vs. $t_{1/2}$ (Fig. 32h) it was found that the adsorption process of Congo red dye using $CoFe_2O_4$@HaP adsorbent occurs in two stages.

Also, the intra-particle diffusion model does not fit the adsorption data, with the corresponding R^2 values for both steps being lower. Therefore, it can be highlighted that the rate-determining step of the Congo red dye adsorption process using $CoFe_2O_4$@HaP adsorbent is determined by chemical adsorption [152, 153].

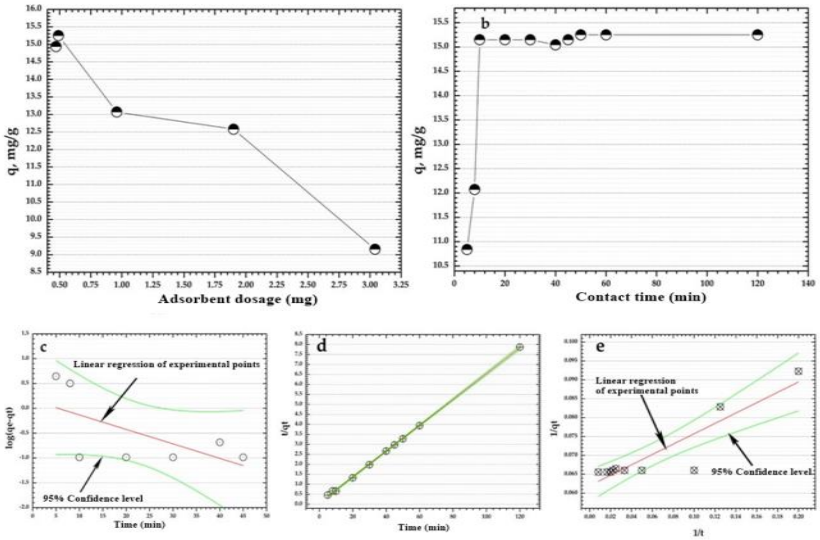

Figure 32. Figure 32. (a) Effect of $CoFe_2O_4$@HaP dosage on dye adsorption; (b) Effect of contact time on dye adsorption; (c) Pseudo one-order kinetic model plot; (d) Pseudo two order kinetic model plot, Type 1; (e) Pseudo two order kinetic model plot, Type 2 [158]

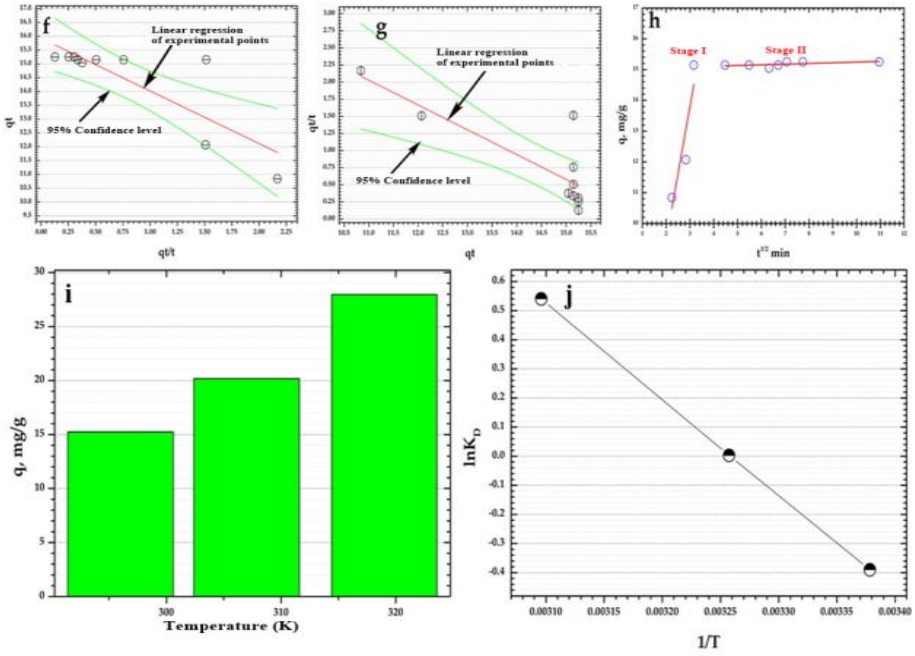

Figure 32. (f) Pseudo second order kinetic model plot, Type 3; (g) Pseudo second order kinetic model plot, Type 4; (h) Intraparticle diffusion model plot; (i) Effect of temperature on dye adsorption; (j) Van't Hoff plot of dye adsorption on $CoFe_2O_4$@HaP adsorbent [158]

The presentation of the kinetic parameters for the investigated models (Fig. 32 c-h) calculated from the slope and intercept using the equations from the specialized literature [154, 155] are listed in table 7.

Table 7. Kinetic parameters [158]

The kinetic model	Equation	result
Pseudo-first order kinetic model	$\log(q_e - q_t) = \log q_e - \frac{(k_1 t)}{2.303}$	k_1 = 0.0672 R^2 = 0.399
Pseudo-second order kinetic model, type 1	$\frac{t}{q_t} = \frac{1}{k_2 {q_e}^2} + \frac{t}{q_e}$	q_e = 15.74 k_2= 0.0416 R^2 = 0.9984
Pseudo-second order kinetic model, type 2	$\frac{1}{q_t} = \left(\frac{1}{k_2 q_e^2}\right)\frac{1}{t} + \frac{1}{q_e}$	q_e = 16.39 k_2= 0.0256 R^2 = 0.8334
Pseudo-second order kinetic model, type 3	$q_t = q_e - \left(\frac{1}{k_2 q_e^2}\right)\frac{q_t}{t}$	q_e = 16.13 k_2= 0.1267 R^2 = 0.6829
Pseudo-second order kinetic model, type 4	$\frac{q_t}{t} = k_2 q_e^2 - k_2 q_e^2 q_t$	q_e = 17.02 k_2= 0.0196 R^2 = 0.6829
Intra-particle diffusion model, Stage 1	$q_t = K_{ID} t^{0.5} + C$	Stage 1: K_{ID} = 4.352 C= 0.7516 R^2 = 0.8467
		Stage 2: K_{ID} = 0.0176 C= 15.042 R^2 = 0.0639

From table 7 it can be seen that the optimal value for the correlation coefficient R^2 was obtained in the case of the Type 1 pseudo second-order kinetic model (R^2 = 0.9984). The calculated adsorption capacity (q_e cal) had the highest value for the Type 4 pseudo second-order kinetic model (q_e cal = 17.02 mg/g). The type of adsorption process was established based on the thermodynamic parameters Gibbs free energy (ΔG°), entropy change (ΔS°) and enthalpy change (ΔH°), Equations 4 and 5 [156]. The ΔH° and ΔS° parameters were determined from the slope and intercept of the $\ln K_D$ vs. 1/T (Fig. 32j).

$$lnK_D = \frac{\Delta S^0}{R} - \frac{\Delta H^0}{RT} \quad (4)$$

$$\Delta G = -RTlnK_D \quad (5)$$

The parameter ΔH° showed that the adsorption process is endothermic. The negative values of ΔG° obtained for all three temperatures indicate the spontaneity and feasibility of the adsorption process. The affinity of the $CoFe_2O_4$@HaP adsorbent for Congo red dye adsorption is evidenced by the positive values of ΔS°. Adsorption isotherm study was deduced using Langmuir and Freundlich isotherms (Fig. 33).

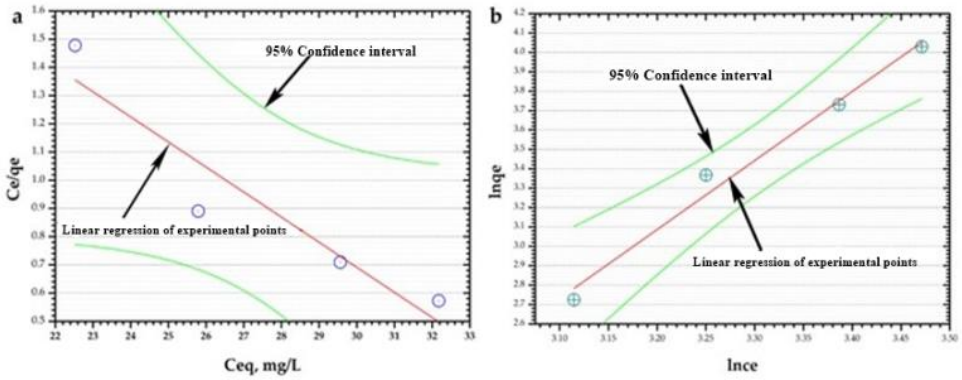

Figure 33. (a) Langmuir isotherm model; (b) Freundlich isotherm model [158]

Evaluating R^2, the correlation coefficient, of both models, the Freundlich model was observed to fit the adsorption data with an R^2 value of 0.9844. To establish the ability of the $CoFe_2O_4$@HaP composite to be reused, three adsorption/desorption cycles were performed. A 0.1 M HNO_3 solution was used for the desorption study.

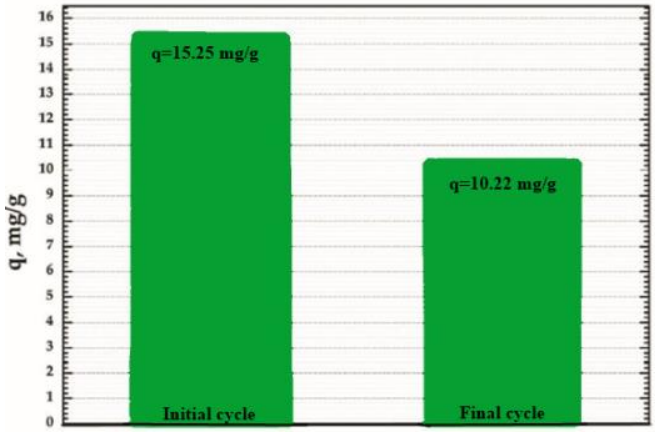

Figure 34. Direct comparison of the adsorption capacity (q, mg/g) after reuse of the adsorbent in relation to the initial cycle versus the final cycle [158]

The obtained results (Fig. 34) show that the $CoFe_2O_4$@HaP composite can be reused as an adsorbent for the proposed dye, the adsorption capacity being 10.22 mg/g after the final reuse cycle [158].

III.4. Study of ibuprofen adsorption on $CuFe_2O_4$ and $CuFe_2O_4$@HaP sorbents

In this subchapter we aimed to determine the capacity of $CuFe_2O_4$ and $CuFe_2O_4$@HaP sorbents to encapsulate ibuprofen from an aqueous solution by adsorption, with the aim of comparing the results obtained with the values determined and presented by Hassanzadeh-Tabrizi and colleagues [21] on a $CoFe_2O_4$@HaP sample in the literature. To choose the concentration value for the ibuprofen stock solution, a calibration curve was performed on a concentration range of 13, 18, 24 and 30 mg/L. The 30 mg/L concentration solution gave the highest absorbance value, from the analyzed series, and thus the absorption studies were performed for this solution.

In order to observe the influence of the contact time on the adsorption process, a series of experiments was carried out and the obtained results are presented below. From the ibuprofen stock solution (30 mg/L) 25 mL was taken, over which 25 mg of sorbent ($CuFe_2O_4$ and $CuFe_2O_4$@HaP) and 25 mL ethanol was added. The time interval in which the solution containing the drug was put in contact with the sorbent was 24, 48 and 72 hours. Working protocol modified according to the bibliographic reference [21]. The influence of the contact time on the adsorption, experimental result can be found in the graphs in figure 37.

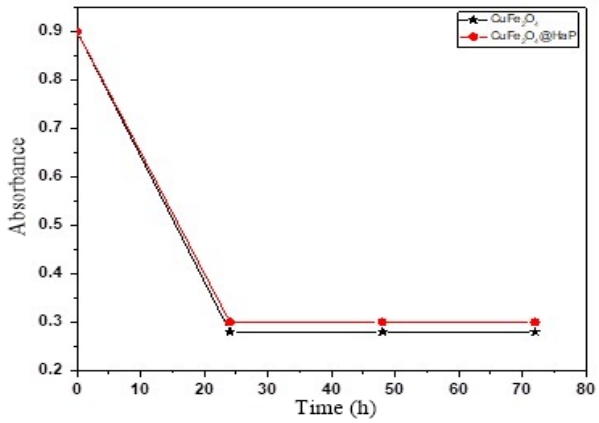

Figure 37. The influence of contact time on the adsorption process of ibuprofen on $CuFe_2O_4$ and $CuFe_2O_4$@HaP sorbents.

After analyzing the graphs in figure 37, it was observed that after 24 hours the absorbance of the solution decreased, after which a level was recorded until the last measurement at 72 hours. The best percentages obtained were 41.72% in the case of the $CuFe_2O_4$ sorbent and 53.83% respectively for the $CuFe_2O_4$@HaP sorbent.

In order to check whether ibuprofen was adsorbed and is part of the composition of the sorbents, a series of FT-IR analyzes were performed for the samples of: ibuprofen (IBU), $CuFe_2O_4$, $CuFe_2O_4$@HaP. The spectra are shown in figure 38.

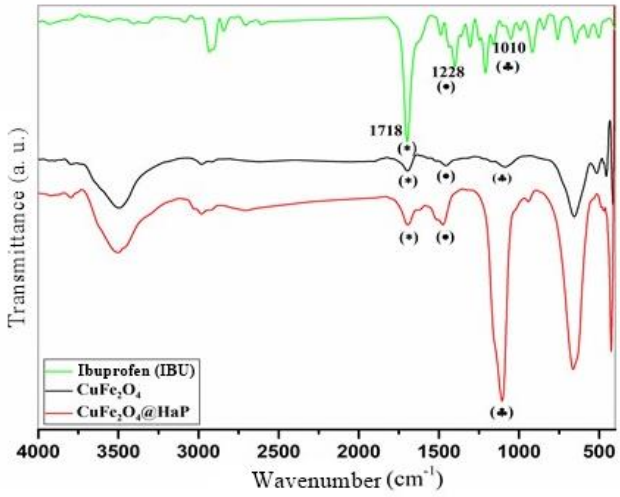

Figure 38. FT-IR spectra for ibuprofen samples (IBU), $CuFe_2O_4$, $CuFe_2O_4$@HaP

The structure of pure ibuprofen (Fig. 38) showed characteristic sharp absorption bands at 1718 cm^{-1}, representing the functional group (COOH) of the carboxylic acid in the structure of ibuprofen and on the interval 1228 - 1010 cm^{-1} bands corresponding to the benzene ring in the composition of the drug [167]. These bands were also observed in the structures of the sorbents used, so it can be stated that ibuprofen was adsorbed by them from the tested solution.

IV. Study of the enzymatic coupling of α-glucosidase to the $MgFe_2O_4$@HaP@APTES nanocomposite

Over the years, nanoparticles, nanocomposites as well as other nanodimensional compounds have been the focus of many research studies, especially for the delivery and drug identification [168-172], as well as in the development of bioassays by improving working techniques [174]. Particular attention has been paid to nanoparticles coupled with enzymes in biotechnological applications [175] and in the identification of new ligands [176, 177].

The choice of $MgFe_2O_4$@HaP nanocomposite in this study represents a continuity of the results of the research group in which we activated [125, 158] with modifications by introducing hydroxyapatite (HaP) into the magnesium ferrite structure (subchapter III.1.2).

In this study, the enzymatic activity of α-glucosidase was tested following the interaction with a magnesium ferrite and hydroxyapatite nanocomposite amino-functionalized - $MgFe_2O_4$@HaP@APTES, with the aim of using the obtained new product in the identification of old or new enzyme inhibitors to be used in various biomedical applications.

IV.1. Synthesis of compounds

IV.1.1. Synthesis of $MgFe_2O_4$@HaP@APTES

The need for the presence of the amino functional group on the surface of ferrites to allow their use in enzymatic applications was the basis of this study.

The amino functionalization procedure consisted of: the mixture consisting of - 0.5 grams of magnesium ferrite and hydroxyapatite ($MgFe_2O_4$@HaP) synthesized according to the protocol in subchapter III.1.2, were dispersed in 30 mL absolute ethanol, 1 mL APTES 2% and 30 mL distilled water - was mechanically stirred for 2 hours at 343.15K. After this time interval the particles were washed three times with absolute ethanol and dried in an oven for 24 hours at 343.15K [188].

IV.1.2. Enzymatic coupling of $MgFe_2O_4$@HaP@APTES nanoparticles by α-glucosidase

A suspension of $MgFe_2O_4$@HaP@APTES is washed three times with 1 mL of pyridine buffer solution (10 mM), over which 0.15 mL of 25% glutaraldehyde solution is added and incubated for 12 hours in a thermoblock preset to 310.15K. The nanoparticles are separated by decantation or centrifugation and washed three times with 1 mL of pyridine buffer. Then add the solution of 0.15 mL α-glucosidase (27.6 U/mL) over the activated particles and incubate again for 12 hours. The nanoparticles are separated and suspended in 0.15 mL of 0.1 M hydroxylamine solution and incubated for another 12 h. Finally, the nanoparticles are separated and washed with 1 mL of saline phosphate buffer solution (10 mM) and kept in the same solution at 277.15K. Protocol adapted from those proposed in the bibliographic references [178, 190].

IV.2. Working protocol for determining the enzymatic activity of α-glucosidase following the interaction with the functionalized amino nanocomposite

Activity of α-glucosidase was tested using 4-nitrophenyl-α-D-glucopyranoside (pNPG) as a substrate. In this reaction, α-glucosidase catalyzes the hydrolysis of glycosidic bonds in the substrate, with the formation of α-D-glucopyranoside and p-nitrophenol (p-NP) who can be measured spectrophotometrically at 405 nm [191 - 193].

IV.3. Characterization of synthesized samples

IV.3.1. X-ray Diffraction (XRD)

To determine the structureand the phases of the synthesized samples were analyzed by X-ray powder diffraction. Figure 40 shows the results obtained for the $MgFe_2O_4$, $MgFe_2O_4$@HaP and $MgFe_2O_4$@HaP@APTES samples.

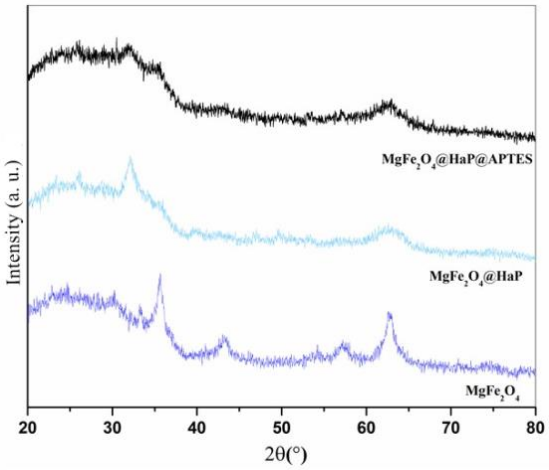

Figure 40. Diffractograms of $MgFe_2O_4$, $MgFe_2O_4$@HaP and $MgFe_2O_4$@HaP@APTES samples

For the $MgFe_2O_4$ sample, the XRD results indicate the presence of a single phase characteristic of a cubic spinel type structure, space group *Fd-3m* [ICSD 98-004-9135], the nanocomposite of magnesium ferrite and hydroxyapatite - $MgFe_2O_4$@HaP presents in addition to the spinel phase cubic of ferrite [ICSD 98-002-4085] and a structure of hexagonal type characteristic of hydroxyapatite with space group *P63/3m* [ICSD 98-009-4278]. Amino functionalization of the $MgFe_2O_4$@HaP nanocomposite did not lead to changes in its crystal structure.

IV.3.2. FT-IR spectroscopy

Data regarding the nature of molecular bonds and functional groups present in the structure of the samples were obtained by infrared spectroscopy

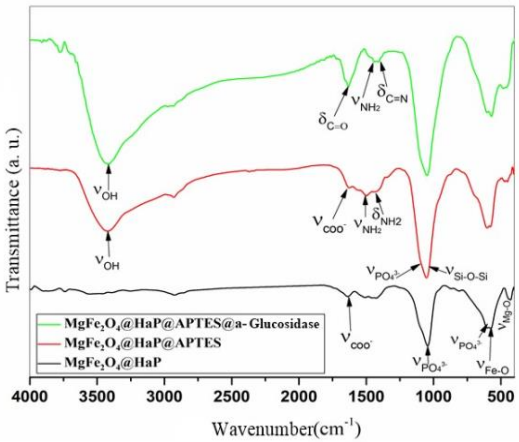

Figure 41. FT-IR spectra of $MgFe_2O_4$, $MgFe_2O_4$@HaP and $MgFe_2O_4$@HaP@APTES samples [196]

Absorption bands corresponding to Si-O-Si groups in the $MgFe_2O_4$@HaP@APTES, nanocomposite was observed at 1041 cm^{-1}. The amino group $–NH_2$ from the structure of the nanocomposite as well as from that of the enzyme was identified at 1645 cm^{-1} (δ_{NH_2}). After the reaction between the amino groups of α-glucosidase and the C=O groups of the glutaraldehyde linker, two typical absorption bands of the protein were observed at 1726 ($\delta_{C=O}$) and 1522 cm^{-1} ($\delta_{C=N}$), demonstrating that the enzyme was successfully integrated into the structure of the nanocomposite [197].

IV.3.3. Analysis of the morphology and composition of the samples by SEM and EDX

To observe the morphological and compositional characteristics of the samples synthesized for this study, scanning electron microscopy (SEM) and energy dispersive X-ray spectroscopy (EDX) analyzes were performed. SEM images for the $MgFe_2O_4$, $MgFe_2O_4$@HaP and $MgFe_2O_4$@HaP@APTES samples are found in figure 42 (a, b, c).

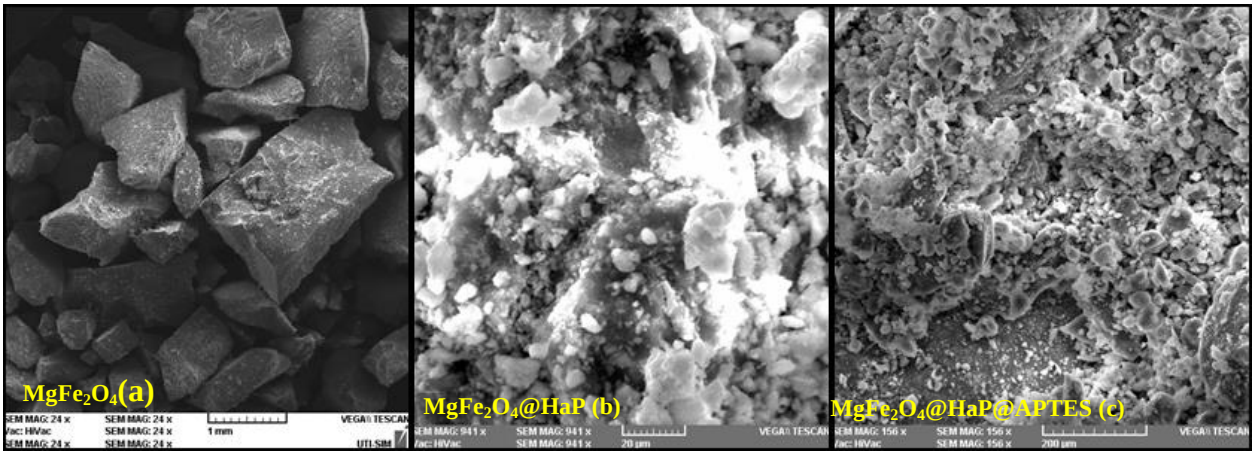

Figure 42. SEM images of $MgFe_2O_4$ (a), $MgFe_2O_4$@HaP (b) and $MgFe_2O_4$@HaP@APTES (c) samples

In the SEM image for the magnesium ferrite sample (Fig. 42(a)), it appears as agglomerated and uneven distribution. In the case of magnesium ferrite and hydroxyapatite nanocomposite (Fig. 42(b)), the formation of a hydroxyapatite layer over the ferrite nanoparticles is observed. Covering the nanocomposite with APTES (Fig. 42(c)), did not change its surface. After analyzing the samples and by energy dispersive X-ray spectroscopy (EDX), the elements

corresponding to the structures were identified. Figures 43-47 show the images and spectra with the obtained results.

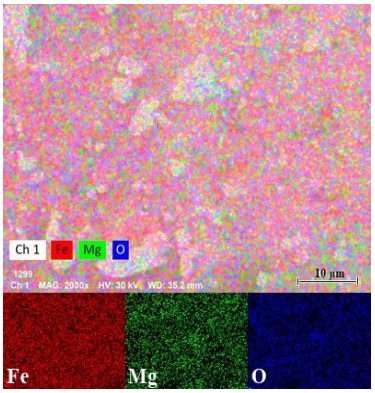

Figure 43. EDX images of the $MgFe_2O_4$ sample

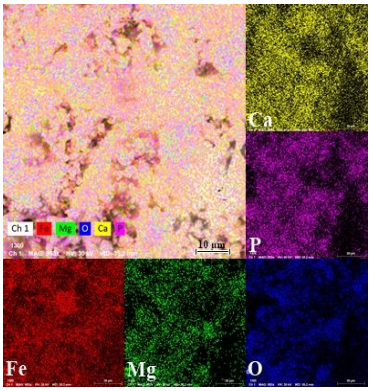

Figure 44. EDX images of the $MgFe_2O_4$@HaP sample

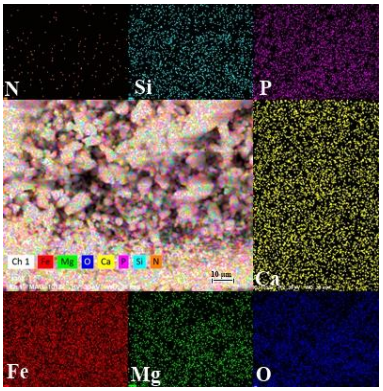

Figure 45. EDX images of the $MgFe_2O_4$@HaP@APTES sample

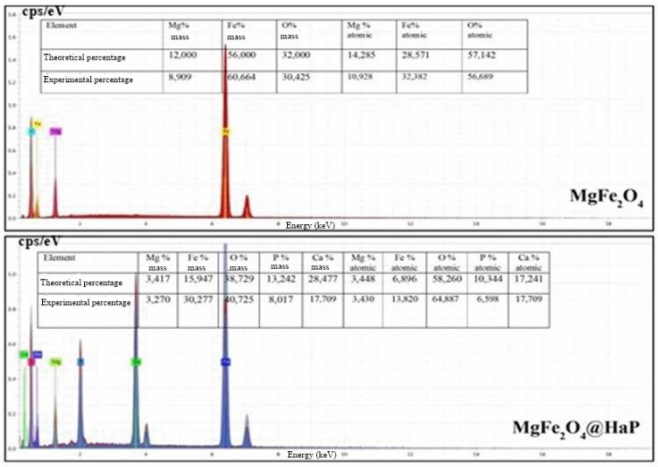

Figure 46. EDX spectrum for the $MgFe_2O_4$ sample and for the $MgFe_2O_4$@HaP sample

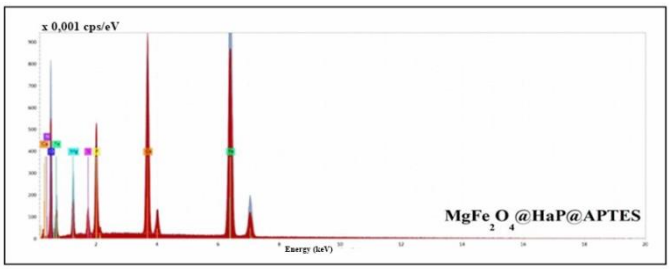

Figure 47. EDX spectrum for the $MgFe_2O_4$@HaP@APTES sample

The EDX images in figure 43 - 45 confirm the presence of specific elements in the structures of the analyzed samples. The EDX spectra in figures 46 - 47 following the assignment of the energy maxima to the corresponding elements, reconfirmed the obtaining of magnesium ferrite and $MgFe_2O_4$@HaP and $MgFe_2O_4$@HaP@APTES nanocomposites.

IV.3.4. Textural analyzes by the BET technique

Analysis of nitrogen adsorption-desorption processes was performed to characterize the pore texture of the synthesized materials. Figure 48 (a, b, c) shows the characteristic isotherms of the analyzed samples, as well as the distributions corresponding to the pores.

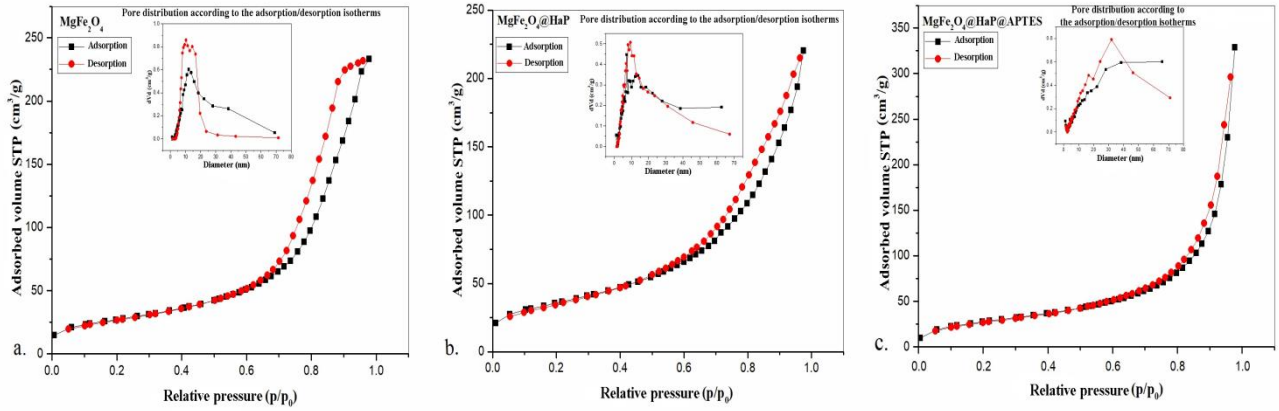

Figure 48. Adsorption-desorption isotherms and pore distributions for the analyzed samples: a) $MgFe_2O_4$; b) $MgFe_2O_4$@HaP; c) $MgFe_2O_4$@HaP@APTES [196]

For all analyzed samples, the adsorption isotherms shows the appearance of a type IV isotherm according to the IUPAC classification [87], with a capillary condensation at high relative pressures, characteristic of mesoporous materials. The textural parameters resulting from processing the adsorption-desorption isotherms, as well as the specific surface area and the total pore volume for the synthesized samples are shown in table 9

Table 9. The textural properties of the synthesized nanocomposites [196]

No.	Sample	Specific surface area ($m^{2/}g$) S_{BET}	Total pore volume (cm^3/g)	Pore diameter (nm) (BJH)
1	$MgFe_2O_4$	96	0.345	11
2	$MgFe_2O_4$@HaP	125	0.300	15
3	$MgFe_2O_4$@HaP@APTES	84	0.350	30

As seen in Table 9, the BET specific surface areas and pore volumes with the highest values are 125 m^2/g ($MgFe_2O_4$@HaP) and 0.35 cm^3/g ($MgFe_2O_4$@HaP@APTES), respectively. Regarding the pore diameter, the values obtained for the three samples fit them as a size in the mesopore range, and the sample with the smallest diameter is that of $MgFe_2O_4$ [197]. The amino functionalization process led to a decrease in the specific surface area and an increase in the pore diameter for the nanocomposite, by introducing some amino groups on the surface of the compound, which implies an increase in the mass of the sample and thus a part of the pore volume is occupied [201].

IV.3.5. Magnetic properties

Magnetic behavior of $MgFe_2O_4$, $MgFe_2O_4$@HaP samples was investigated by the Vibrating Sample Magnetometry (VSM) technique. M-H hysteresis loops were recorded in the ±10 kOe range (Fig. 49) and by means of them specific magnetic parameters such as saturation magnetization (M_s), remanent magnetization (M_r), coercivity (H), M_r/M_s ratio were determined and are shown in Table 10.

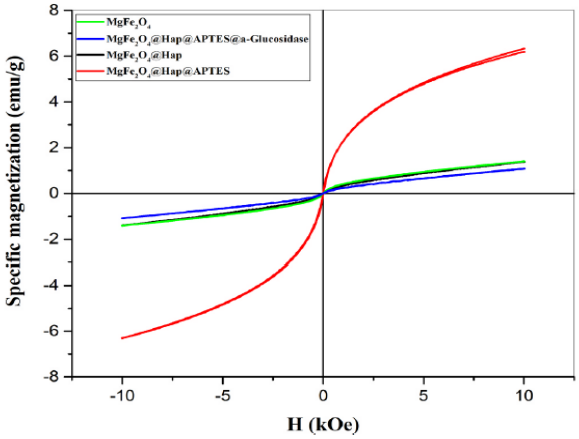

Figure 49. Hysteresis loops of synthesized samples [196]

As expected, the introduction of magnesium ferrite into the hydroxyapatite structure led to the modification of the initially calculated parameters. The decrease in the magnetization value of the nanocomposite compared to that of the simple ferrite could be induced by the masking of the magnetic component in the hydroxyapatite material during the synthesis process. Also, the amino functionalization of the nanocomposite resulted in obtaining a slightly lower

value of the saturation magnetization, compared to the simple ferrite sample, caused by the presence of amino groups that are non-magnetic [202]. In addition, enzyme coupling to the nanocomposite did not lead to loss of magnetic properties, suggesting that the enzyme-coupled nanocomposite is suitable for applications requiring magnetic separation (Table 10).

Table 10. Magnetic parameters for synthesized samples [196]

No.	**Sample**	**M_r (emu/g)**	**M_s (emu/g)**	**H (kOe)**	**M_r/M_s**
1	$MgFe_2O_4$	0.01	6.31	5.12	0.07
2	$MgFe_2O_4$@HaP	0.04	1.39	2.99	0.02
3	$MgFe_2O_4$@HaP@APTES	0.06	6.25	5.02	0.009
4	$MgFe_2O_4$@HaP@APTES@ α-glucosidase	0.06	6.25	5.02	0.009

Ratio M_r/M_s is less than 0.5 in all samples, which suggests that the analyzed samples interact through magnetostatic interactions [202].

IV.4. Enzyme activity study

IV.4.1. Quantification of primary amino groups on the surface of the nanocomposite

Glycine standard solutions were prepared to construct the calibration curve. The range of concentrations was between 0.25 – 1.75 mM. In a 2 mL microtube (final volume), 1 mL glycine solution was added and brought to a temperature of 353.15K in a water bath. Once the solution reached the set temperature, 100 microliters of reagent solution were added (the coloration appears instantly) and it was left for 20 minutes in the water bath. After this time, samples are taken from the water bath, 900 microliters of 60% ethanol are added, the solution is cooled and the absorbance is measured at 570 nm using a spectrophotometer. In the last experiment, a sample containing a suspension of $MgFe_2O_4$@HaP@APTES nanoparticles was also made, for which the same working conditions were observed and an absorbance value at a wavelength of 570 nm of 0,9 was obtained. The results showed an average absorbance equal to 0.9333 ± 0.02 (measurements were performed in triplicate, ±0.02 representing the standard error of the mean (ESM) at a 95% confidence level). The UV-Vis spectrum of the solution with the $MgFe_2O_4$@HaP@APTES nanoparticle sample is shown in the graph in figure 50.

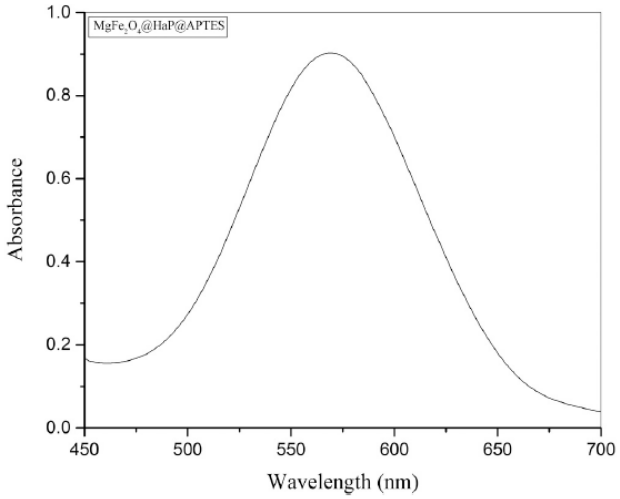

Figure 50. UV-Vis spectrum for the reagent solution containing the $MgFe_2O_4$@HaP@APTES sample [196]

In order to determine (with approximation) the value of the concentration of primary amino groups in the structure of magnesium ferrite and amino hydroxyapatite nanoparticles functionalized with APTES by interpolation, a calibration curve was made for a 10 mM glycine stock solution. The approximate concentration of primary amino groups on the surface of amino-functionalized magnesium ferrite and hydroxyapatite nanoparticles obtained according to the calibration curve is 0.798 mM, corresponding to approximately 239.4 μmol amino groups/g of nanoparticles. The calculation to determine the degree of coverage of the $MgFe_2O_4$@HaP@APTES nanocomposite with amino groups was performed according to Karade et al. [188] and Sun et al. [203] respectively, and a value of 42.91% was obtained. The results show the successful amino functionalization of $MgFe_2O_4$@HaP@APTES nanocomposite using APTES.

IV.4.2. Determination of the enzymatic activity of α-glucosidase following the interaction with the functionalized amino nanocomposite

The enzymic activity of α-glucosidase was determined based on the glycosidic bond cleavage reaction in the substrate 4-nitrophenyl α-D-Glucopyranoside (pNPG). Following the reaction, the substrate is completely converted to p-nitrophenol, which can be determined spectrophotometrically at 405 nm. In this sense, the enzymatic activity of both the simple α-glucosidase and the nanocomposite of the type - $MgFe_2O_4$@HaP@APTES@α-Glucosidase were studied. A mean absorbance value of 0.39 ± 0.03 (N = 3, SEM at 95% confidence level) at 405 nm was obtained for single enzyme in the enzyme activity assay. The immobilized enzyme gave a mean absorbance of 0.2367 ± 0.07 (N = 3, SEM at the 95% confidence level), a value lower than that obtained for the uncoupled enzyme (Fig. 52).

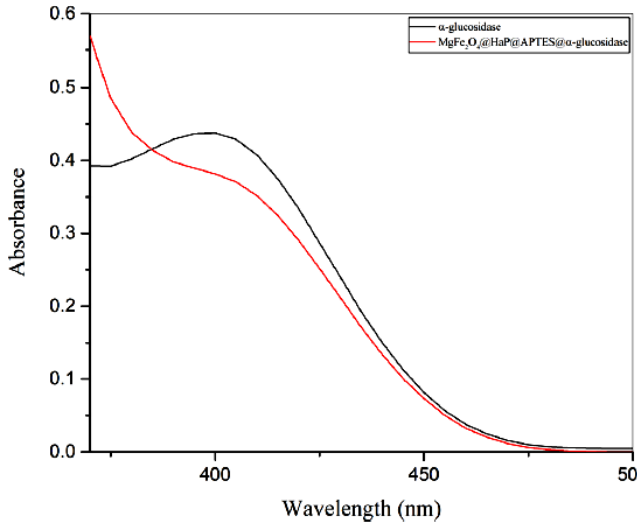

Figure 52. UV-Vis spectra of α-glucosidase and $MgFe_2O_4$@HaP@APTES samples [196]

Based on the obtained results and the spectrum in Figure 52, it can be deduced that α-glucosidase retains its enzymatic activity even after coupling to the nanocomposite. Thus, the enzyme-coupled nanocomposite could be a useful tool in studies aimed at identifying α-glucosidase inhibitors [196].

V. Mixed ferrites of the type $Co_{1-x}Zn_xFe_2O_4$ and $Mn_{1-x}Zn_xFe_2O_4$ coated with Ag (x = 0.5 - 0.1)

V.1. Synthesis of mixed ferrites of the type $Co_{1-x}Zn_xFe_2O_4$ and $Mn_{1-x}Zn_yFe_2O_4$ (x = 0.5 - 0.1)

Mixed ferrites of the type $Co_{1-x}Zn_xFe_2O_4$ and $Mn_{1-x}Zn_xFe_2O_4$ were obtained by the co-precipitation method in aqueous solution. The amounts and types of precursors used in the synthesis can be found in Table 11.

Table 11. The amounts of precursors used in the synthesis of the two series of mixed ferrites

Mixed ferrites	$CoCl_2•6H_2O$(g)	$FeCl_3•6H_2O$(g)	$ZnCl_2$(g)
$Co_{0.5}Zn_{0.5}Fe_2O_4$	2.498	11.44	1.42
$Co_{0.6}Zn_{0.4}Fe_2O_4$	3.006	11.44	1.14
$Co_{0.7}Zn_{0.3}Fe_2O_4$	3.516	11.44	0.86
$Co_{0.8}Zn_{0.2}Fe_2O_4$	4.03	11.44	0.573
$Co_{0.9}Zn_{0.1}Fe_2O_4$	4.544	11.44	0.28
	$MnCl_2•6H_2O$	$FeCl_3•6H_2O$	$ZnCl_2$
$Mn_{0.5}Zn_{0.5}Fe_2O_4$	2.096	11.44	1.44
$Mn_{0.6}Zn_{0.4}Fe_2O_4$	2.526	11.44	1.14
$Mn_{0.7}Zn_{0.3}Fe_2O_4$	2.96	11.44	0.86
$Mn_{0.8}Zn_{0.2}Fe_2O_4$	3.398	11.44	0.582
$Mn_{0.9}Zn_{0.1}Fe_2O_4$	3.84	11.44	0.292

The work protocol used was adapted from that proposed in the bibliographic reference [125].

V.2. Characterization of mixed ferrites synthesized by the type $Co_{1-x}Zn_xFe_2O_4$ and $Mn_{1-x}Zn_xFeO_4$ (x = 0.5 - 0.1)

The structural properties of the samples synthesized in this study were characterized by FT-IR spectroscopy and XRD diffraction, and the magnetic properties were investigated by VSM measurements.

V.2.1. X-ray Diffraction (XRD)

By analyzing the two series of mixed ferrites using X-ray diffraction, information on the crystal structure, phase purity and crystallite size corresponding to each sample could be identified. The diffractograms recorded for the series of mixed ferrites are shown in figures 53 and 54.

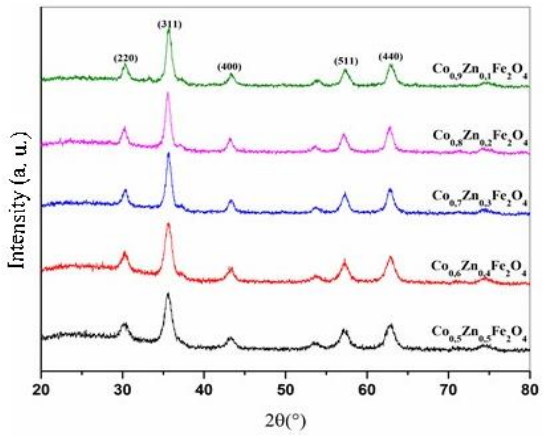

Figure 53. XRD diffractograms for the $Co_{1-x}Zn_xFe_2O_4$ series, (x = 0.5-0.1)

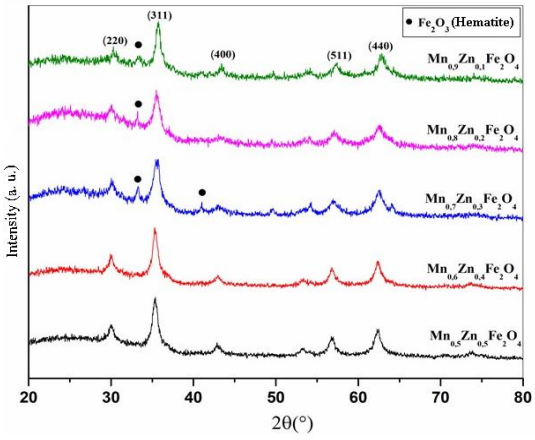

Figure 54. XRD diffractograms for the $Mn_{1-x}Zn_xFe_2O_4$ series, (x = 0.5-0.1)

After analyzing the diffraction maxima observed the phase formation corresponding to cubic spinel-type ferrites, space group *Fd-3m* as well as the secondary phase characteristic of the hexagonal structure of hematite were observed, which were assigned to the ICSD [98-008-8612], ICSD [98-006-3176] and ICSD [98-005-3779] databases. The crystallite sizes of the mixed ferrites were calculated using the Scherrer equation (eq. 2). The smallest values of the crystallite sizes were obtained for the samples of $Co_{0.5}Zn_{0.5}Fe_2O_4$ and $Mn_{0.8}Zn_{0.2}Fe_2O_4$.

V.2.2. FT-IR spectroscopy

FT-IR spectra provide information about the possible presence of ions in the crystalline structures as well as their vibrational modes. The two series of synthesized mixed ferrites were analyzed and the obtained FT-IR spectra are reproduced in Figures 55 and 56.

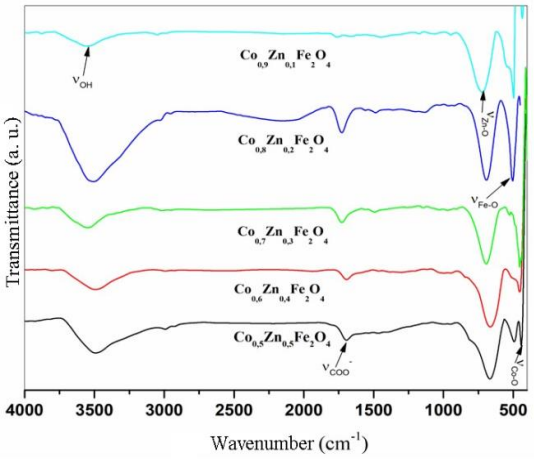

Figure 55. FT-IR spectra for the $Co_{1-x}Zn_xFe_2O_4$, x = 0.5 - 0.1 series

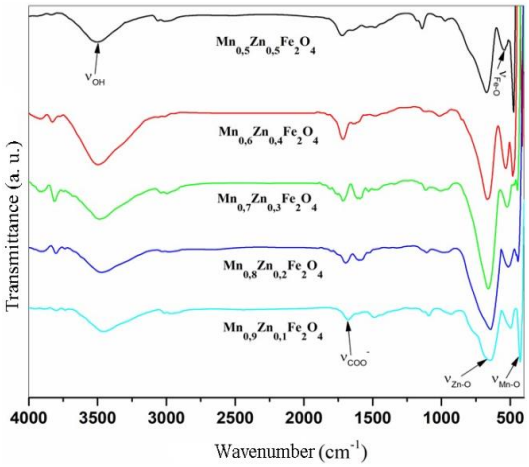

Figure 56. Series FT-IR spectra for the $Mn_{1\ x}Zn_xFe_2O_4$, x = 0.5 - 0.1 series

Following the interpretation of the spectra in Figures 55 and 56, the characteristic absorption bands of the two series of samples were identified and correlated (Table 13).

Table 13. Absorption bands characteristic of the two series of mixed ferrites

No. crt	Wave number (cm^{-1})	Assignments
1	3423-3410	ν_{OH} – absorption bands corresponding to the valence vibrations of the OH group in water molecules
2	1646-1624	ν_{COO^-} - absorption bands corresponding to the valence vibrations of the COO^- bond in the residual CMC molecules
3	601-576	$\nu_M{}^{Td}{}_{-O}$ – absorption bands corresponding to the valence vibrations of the M-O bonds (Zn-O) in the tetrahedral sites (Td) in the ferrite structure
4	455-446	$\nu_M{}^{Oh}{}_{-O}$ – absorption bands corresponding to the valence vibrations of the M-O bonds (Fe – O) in the octahedral sites (Oh) in the ferrite structure
5	397-349	$\nu_M{}^{Oh}$- O – absorption bands corresponding to the valence vibrations of the M-O bonds (Co, Mn – O) in the octahedral sites (Oh) in the ferrite structure

The introduction of zinc, and the redistribution of cations, resulted in a shift of the bands to lower wavenumbers with increasing zinc concentration in the samples. These changes in ferrite structure could be caused by cation redistribution but also by the difference in electronegativity between zinc, manganese and cobalt atoms [204-206].

V.2.3. Analysis of the morphology and composition of mixed ferrite samples by SEM and EDX

To observe the morphology and elemental composition of the two series of mixed ferrites, SEM microscopy and EDX spectroscopy analyses were performed. Figure 57 shows the SEM images obtained. The elemental composition of the plain and silver coated mixed ferrite samples was determined by EDX spectroscopy analysis. The obtained graphs and spectra are shown in Figures 58 and 59.

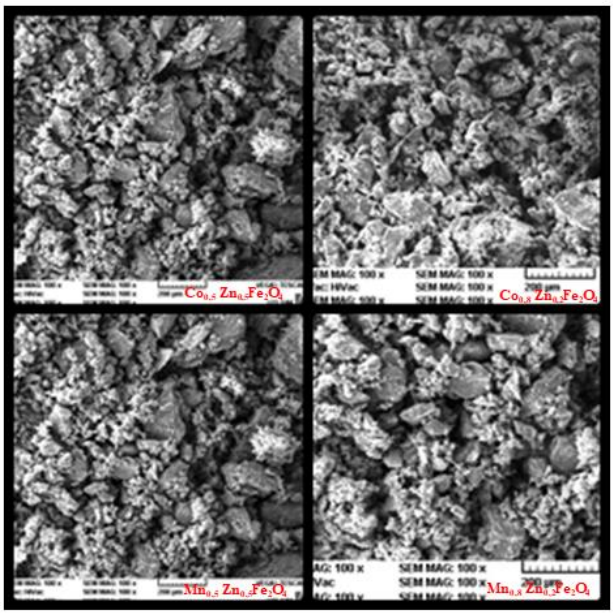

Figure 57. SEM images for $Co_{1-x}Zn_xFe_2O_4$ and $Mn_{1-x}Zn_xFe_2O_4$ samples, (x = 0.5 - 0.1)

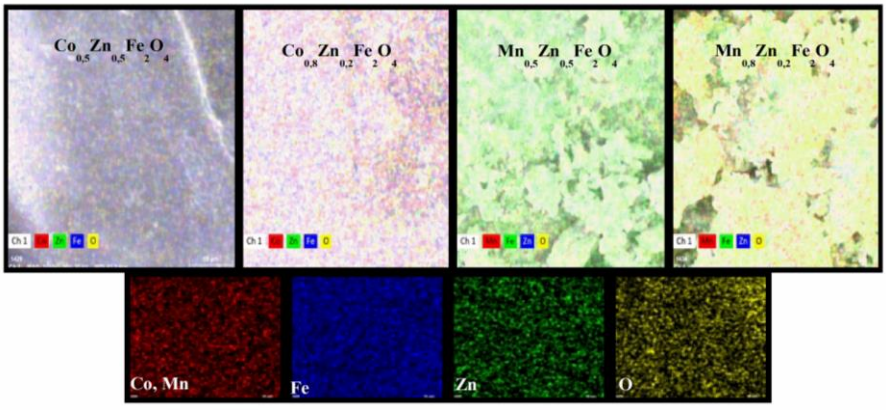

Figure 58. Elemental composition for $Co_{1-x}Zn_xFe_2O_4$ and $Mn_{1-x}Zn_xFe_2O_4$ samples (x = 0.5; 0.2)

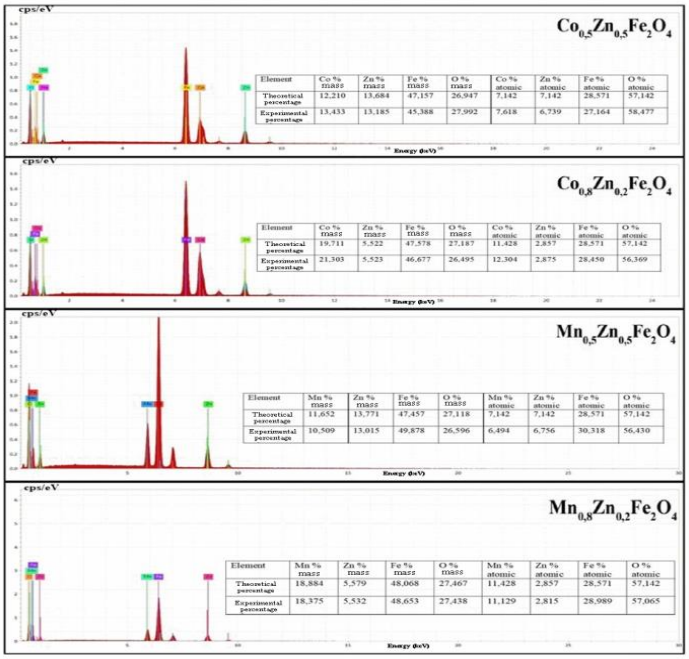

Figure 59. EDX spectra for the $Co_{1-x}Zn_xFe_2O_4$ series and for the $Mn_{1-x}Zn_xFe_2O_4$ series (x = 0.5; 0.2)

From the SEM images in Fig. 57, the morphology of the samples was observed, presented as non-uniformly distributed agglomerates. From the resulting EDX images (Figs. 57-58), elements specific to mixed ferrites could be identified. The values of the elemental compositions obtained by EDX spectroscopy are close to the theoretical values, the differences can be associated with the analysis performed, which is a surface analysis.

V.2.4. Magnetic properties

The magnetic behavior of the two series of mixed ferrites synthesized was analyzed by means of the interpretation of the magnetic hysteresis (M-H) loops, obtained at room temperature, in the range ±12 kOe.

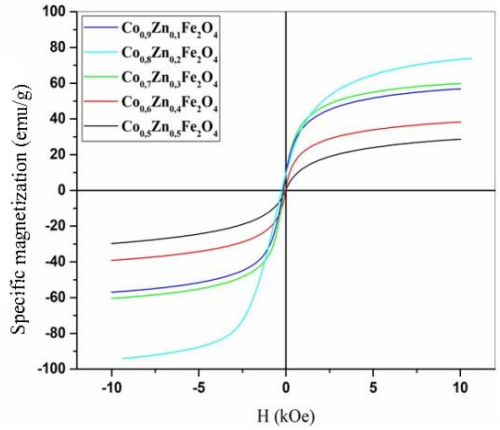

Figure 60. Hysteresis loops for $Co_{1-x}Zn_xFe_2O_4$, (x = 0.1-0.5) ferrite series

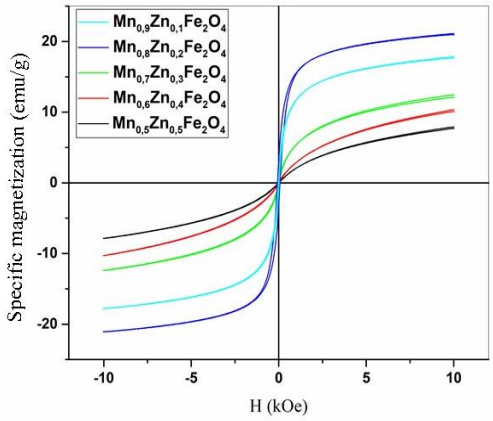

Figure 61. Hysteresis loops for $Mn_{1-x}Zn_xFe_2O_4$, (x = 0.1-0.5) ferrite series

The magnetic parameters (M_r, M_s, H) obtained from the graphs in Figures 60 and 61 are shown in Table 14.

Table 14. The magnetic parameters for the series of mixed ferrites type $Co_{1-x}Zn_xFe_2O_4$, x = 0.5 - 0.1 and $Mn_{1-x}Zn_xFe_2O_4$, x = 0.5 - 0.1

No.	Sample	M_r (emu/g)	M_s (emu/g)	H (kOe)	M_r/M_s
1	$Co_{0.5}Zn_{0.5}Fe_2O_4$	0.48	8.85	0.02	0.05
2	$Co_{0.6}Zn_{0.4}Fe_2O_4$	1.31	20.54	0.02	0.06
3	$Co_{0.7}Zn_{0.3}Fe_2O_4$	8.87	46.35	0.13	0.19
5	$Co_{0.8}Zn_{0.2}Fe_2O_4$	4.70	26.88	0.13	0.17
6	$Co_{0.9}Zn_{0.1}Fe_2O_4$	10.01	49.68	0.16	0.20
7	$Mn_{0.5}Zn_{0.5}Fe_2O_4$	0.05	2.32	0.02	0.02
8	$Mn_{0.6}Zn_{0.4}Fe_2O_4$	0.09	2.88	0.02	0.03
9	$Mn_{0.7}Zn_{0.3}Fe_2O_4$	0.31	5.94	0.02	0.05
10	$Mn_{0.8}Zn_{0.2}Fe_2O_4$	1.21	13.49	0.02	0.08
11	$Mn_{0.9}Zn_{0.1}Fe_2O_4$	3.32	17.14	0.07	0.19

The two series of mixed ferrites belong to the category of soft ferrites, which is confirmed by the shape of the magnetic M-H hysteresis loops and the values for coercivity (Fig. 60, Fig. 61) [39]. As far as the values of magnetic parameters are concerned, changes in the values were observed for both series of ferrites. These changes in saturation magnetization and coercivity for both ferrite series may be influenced by particle sizes, cation redistribution and weak zinc magnetization [205, 206]. The M_r/M_s ratio values in these samples are less than 0.5, so the particles interact through magnetostatic interactions.

V.3. Coating of $Co_{1-x}Zn_xFe_2O_4$ and $Mn_{1-x}Zn_xFe_2O_4$ type ferrites (x = 0.5 - 0.1) with silver

V.3.1. Synthesis of compounds

The coating of mixed ferrites of the type $Co_xZn_yFe_2O_4$ and $Mn_xZn_yFe_2O_4$ with Ag was achieved by reducing Ag from $AgNO_3$ with glucose. Thus, 1.176 g of ferrite was dispersed in 100 mL of water to which 15 mL of $AgNO_3$ solution (2.5%) and 15 mL of carboxymethylcellulose 1% (CMC) were added. The obtained mixture was stirred in an ultrasonic bath for 30 minutes. Then 10 mL of ammonia solution (25%) and 1.1 g of glucose (2×10^{-4} M) were added and stirring was continued for 1 hour. Working protocol modified according to those proposed in the bibliographic references [207, 208].

V.3.2. Characterization of $Co_{1-x}Zn_xFe_2O_4$@Ag and $Mn_{1-x}Zn_xFe_2O_4$@Ag samples (x = 0.5 - 0.1)

V.3.2.1. X-ray Diffraction (XRD)

To check if silver is found in the structure of the samples, they were analyzed by X-ray diffraction. The graphs in figures 62 and 63 show the diffractograms of the series of mixed ferrites coated with silver.

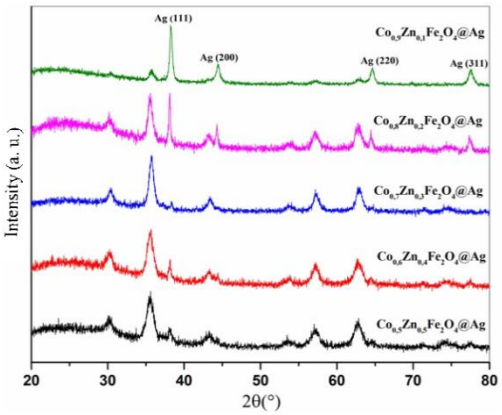

Figure 62. XRD diffractograms for the $Co_{1-x}Zn_xFe_2O_4$@Ag series, x = 0.5 - 0.1

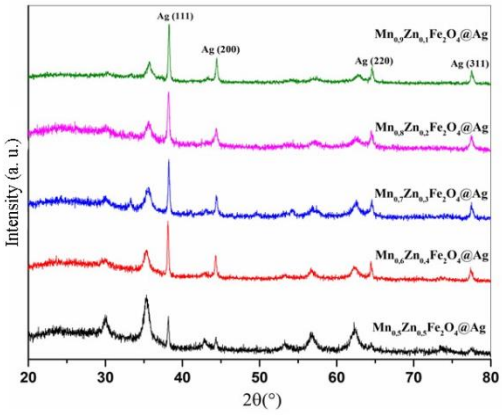

Figure 63. XRD diffractograms for the $Co_{1-x}Zn_xFe_2O_4$@Ag series, x = 0.5 - 0.1

The diffractograms of the samples in figures 62 and 63 show four diffraction maxima at the angle 2Theta – 38.7°; 44.1°; 64.5° and 75.3°, in addition to those corresponding to mixed ferrites. These diffraction maxima, after indexing in the ICSD database [98-002-2068], belong to the reflection planes – (111), (200), (220) and (311), characteristic of metallic silver of cubic symmetry. The crystallite dimensions of the ferrites following silver coating were calculated using the Scherrer equation and are given in Table 15.

Table 15. Crystallite sizes corresponding to the two series of silver-coated mixed ferrites

Sample	Crystallite Sizes (nm)		
	Spinel	Ag	Spinel@Ag
$Co_{0.5}Zn_{0.5}Fe_2O_4$@Ag	12.71	29.30	21.00
$Co_{0.6}Zn_{0.4}Fe_2O_4$@Ag	11.30	21.79	16.54
$Co_{0.7}Zn_{0.3}Fe_2O_4$@Ag	14.07	29.30	21.68
$Co_{0.8}Zn_{0.2}Fe_2O_4$@Ag	16.40	40.80	28.60
$Co_{0.9}Zn_{0.1}Fe_2O_4$@Ag	16.25	36.05	26.15
$Mn_{0.5}Zn_{0.5}Fe_2O_4$@Ag	14.05	34.73	24.39
$Mn_{0.6}Zn_{0.4}Fe_2O_4$@Ag	16.87	45.07	30.97
$Mn_{0.7}Zn_{0.3}Fe_2O_4$@Ag	12.79	52.02	32.40
$Mn_{0.8}Zn_{0.2}Fe_2O_4$@Ag	10.92	31.15	21.03
$Mn_{0.9}Zn_{0.1}Fe_2O_4$@Ag	14.17	50.62	32.39

As can be seen from the crystallite size values in Table 15, compared to the crystallite size values of the uncoated ferrites (Table 12), there was an increase in their value following the coating of the ferrite particles with silver. This can be caused by the increase in the thickness of the silver layer deposited on the surface of the spinels [209].

V.3.2.2. Analysis of the morphology and composition of mixed ferrite samples by SEM microscopy and EDX spectroscopy

Through SEM microscopy and EDX spectroscopy (Fig. 64-66) it was aimed to observe whether silver is found on the surface of mixed ferrites following the coating process.

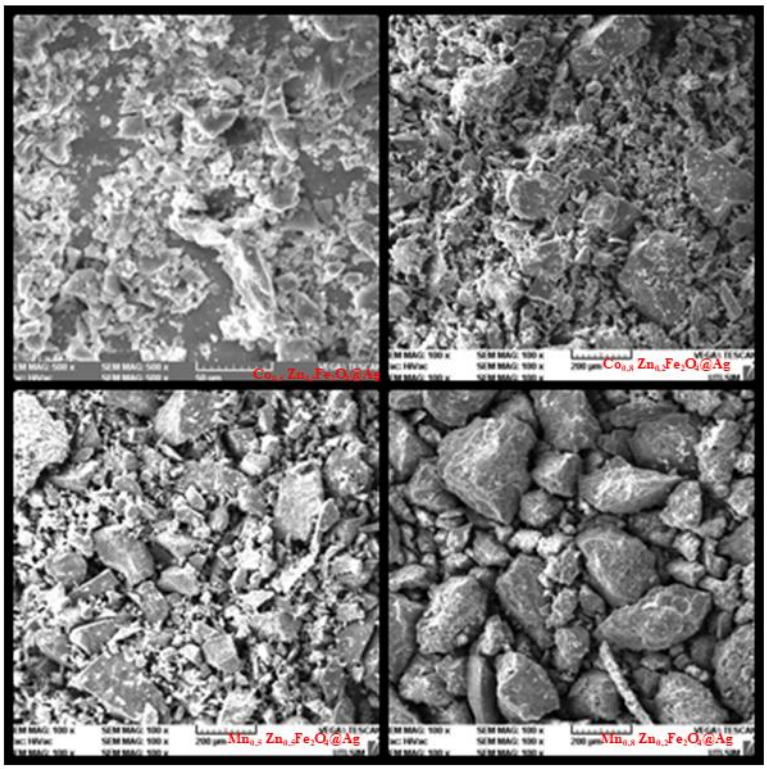

Figure 64. SEM images for $Co_{1-x}Zn_xFe_2O_4$@Ag and $Mn_{1-x}Zn_xFe_2O_4$@Ag(x = 0.5; 0.2) samples

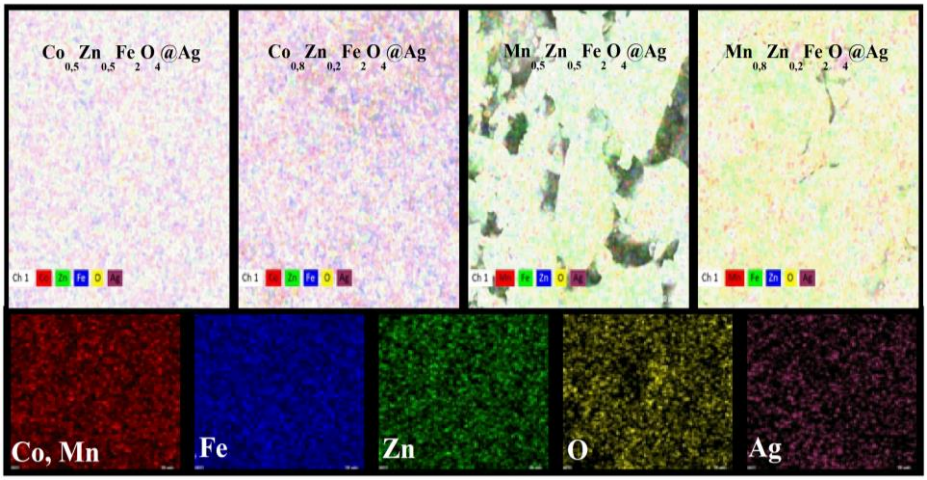

Figure 65. Elemental composition for samples of $Co_{1-x}Zn_xFe_2O_4$@Ag and de $Mn_{1-x}Zn_xFe_2O_4$@Ag (x = 0.5; 0.2)

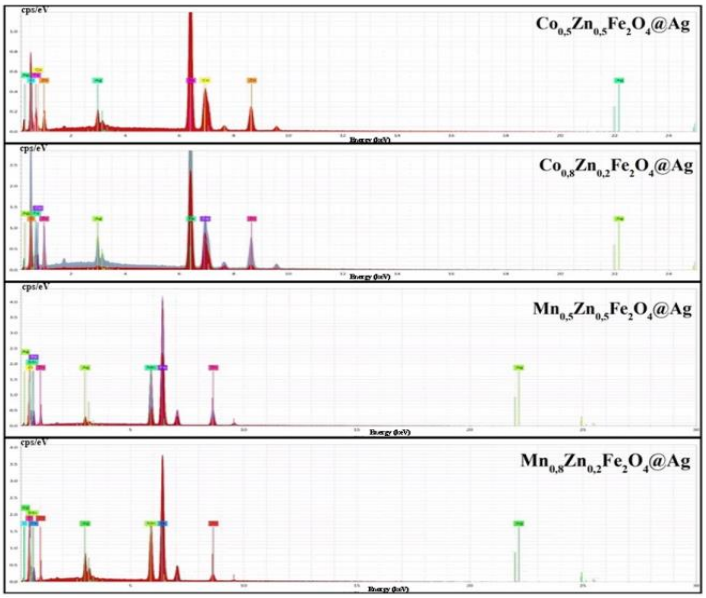

Figure 66. EDX spectra of $Co_{1-x}Zn_xFe_2O_4$@Ag and $Mn_{1-x}Zn_xFe_2O_4$@Ag (x = 0.5; 0.2)

The silver-coated samples (Figure 64) show as agglomerated particles. From the resulting EDX images and spectra, elements specific to mixed ferrites and silver could be identified.

V.3.2.3. Magnetic properties

In the case of using mixed ferrites as potential contrast agents in medical imaging, magnetic properties are very important. For this reason, it was desired to check possible changes in the level of magnetic properties following the coating of mixed ferrites with silver. Figures 67-70 show the magnetization graphs of the samples after silver coating.

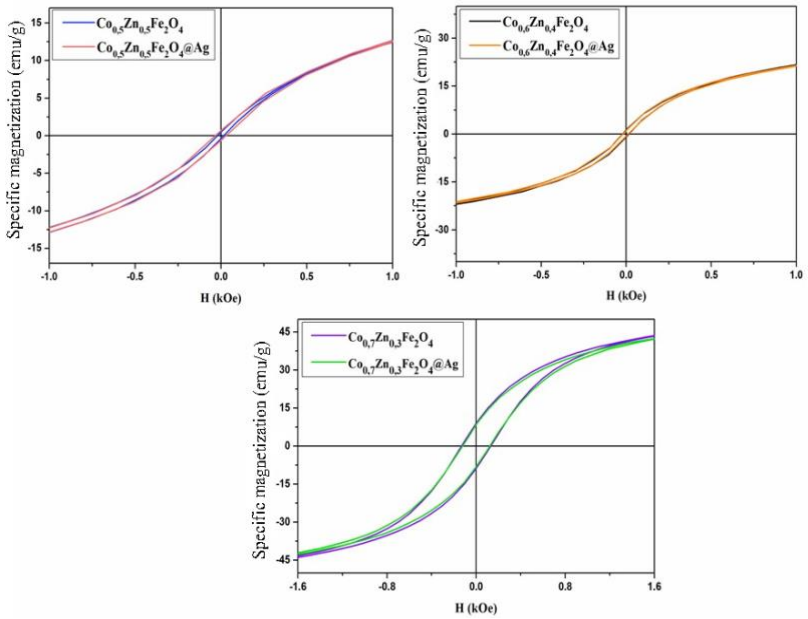

Figure 67. Hysteresis loops for the ferrite series $Co_{1-x}Zn_xFe_2O_4$@Ag, x = 0.5 - 0.3

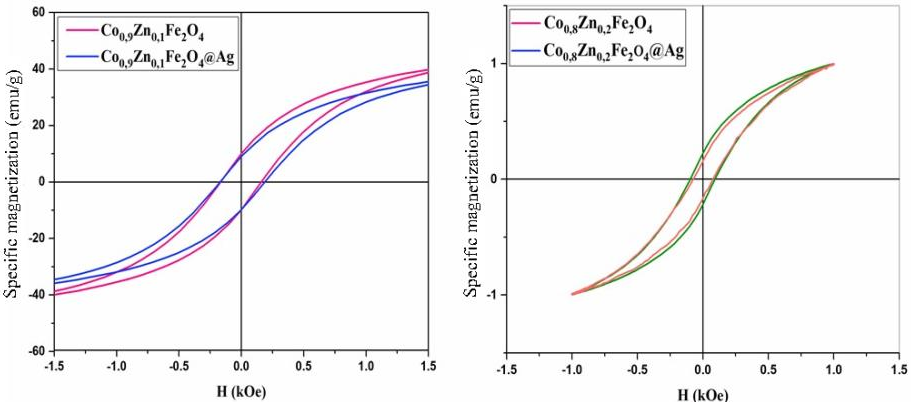

Figure 68. Hysteresis loops for the $Co_{1-x}Zn_xFe_2O_4$@Ag ferrite series, x = 0.1 - 0.2

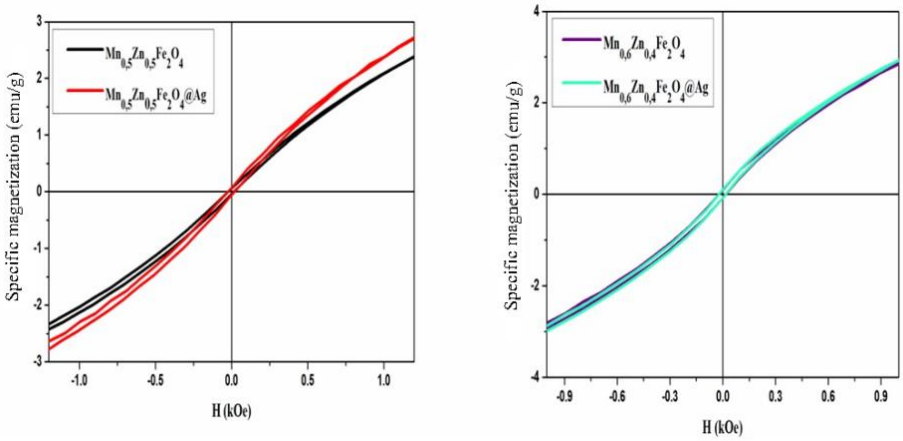

Figure 69. Hysteresis loops for the ferrite series $Mn_{1-x}Zn_xFe_2O_4$@Ag, x = 0.5; 0.4

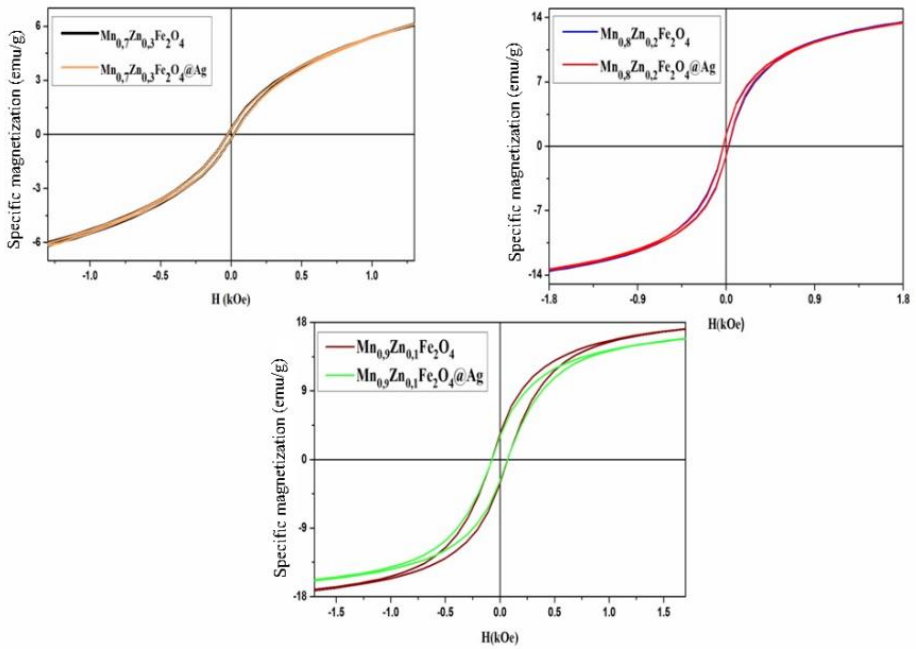

Figure 70. Hysteresis loops for the ferrite series $Mn_{1-x}Zn_xFe_2O_4$@Ag, x = 0.3 - 0.1

The magnetic parameter values corresponding to the silver-coated mixed ferrites were calculated from the hysteresis loops in Figures 67-70. The obtained results are summarized in Table 16.

Table 16. Magnetic parameters for the sample series of $Co_{1-x}Zn_xFe_2O_4$@Ag, x=0.5-0.1 and $Mn_{1-x}Zn_xFe_2O_4$@Ag, x=0.5 - 0.1

No.	Sample	M_r(emu/g)	M_s(emu/g)	H(kOe)	M_r/M_s
1	$Co_{0.5}Zn_{0.5}Fe_2O_4$@Ag	0.69	15.49	0.03	0.04
2	$Co_{0.6}Zn_{0.4}Fe_2O_4$@Ag	1.11	34.36	0.01	0.03
3	$Co_{0.7}Zn_{0.3}Fe_2O_4$@Ag	8.42	47.66	0.12	0.17
5	$Co_{0.8}Zn_{0.2}Fe_2O_4$@Ag	4.00	24.33	0.14	0.16
6	$Co_{0.9}Zn_{0.1}Fe_2O_4$@Ag	9.06	42.09	0.17	0.21
7	$Mn_{0.5}Zn_{0.5}Fe_2O_4$@Ag	0.06	2.37	0.02	0.02
8	$Mn_{0.6}Zn_{0.4}Fe_2O_4$@Ag	0.10	2.88	0.02	0.03
9	$Mn_{0.7}Zn_{0.3}Fe_2O_4$@Ag	0.32	5.94	0.02	0.05
10	$Mn_{0.8}Zn_{0.2}Fe_2O_4$@Ag	1.22	12.36	0.02	0.09
11	$Mn_{0.9}Zn_{0.1}Fe_2O_4$@Ag	2.96	15.08	0.07	0.19

The coating process of the two series of mixed ferrites with silver resulted in small fluctuations of the saturation magnetization values (M_s) and coercivity (H), compared to those of uncoated ferrites (Table 14). The M_r/M_s ratio values remained below 0.5 even after coating, so the particles still interact through magnetostatic interactions.

General conclusions

• Three series of compounds were synthesized in the PhD thesis. The first series comprised magnetic nanoparticles of the MFe_2O_4 ferrite type (M = Co, Cu, Mg, Mn, Ni); in the second series, MFe_2O_4@HaP nanocomposites were obtained consisting of ferrite nanoparticles that were embedded in a hydroxyapatite (HaP) matrix. From this series, the $MgFe_2O_4$@HaP nanocomposite was functionalized with APTES, in order to be α-glucosidase coupled. The third series contained mixed ferrites, $Co_{1-x}Zn_xFe_2O_4$, x = 0.5 - 0.1 and $Mn_{1-x}Zn_xFe_2O_4$, x = 0.5 - 0.1, which were then silver coated. Initially, the experimental conditions used in the synthesis of ferrites were analyzed. The synthesis method by co-precipitation in aqueous solution was chosen, based on the studies carried out in our research group. The properties of hydroxyapatite were studied and then methods to prepare nanocomposites by introducing nanoparticles into its structure were identified. Mixed ferrites were also synthesized by co-precipitation method in aqueous solution.

• The structures and properties of the synthesized compounds were investigated by various analytical methods such as FT-IR spectroscopy, X-ray diffraction, BET and VSM techniques. By FT-IR spectroscopy, ferrite specific M-O bonds were identified in all the synthesized samples. Also the presence of functional groups (PO_4^{3-}) in the hydroxyapatite structure was observed in all nanocomposites. X-ray diffraction helped to determine the cubic spinel structure in the ferrites (*Fd-3m*) and the hexagonal structure (*P63/m*) of hydroxyapatite in the nanocomposites, but the presence of silver was also confirmed after coating the mixed ferrites. BET analysis identified that the samples belong to the mesoporous material category. Textural parameters such as BET specific surface areas and pore volumes were also deduced, the highest values belonging to the samples of: $MgFe_2O_4$, $MgFe_2O_4$@HaP, $NiFe_2O_4$, $NiFe_2O_4$@HaP. For the pore diameter it was observed a classification in the mesoporous class, the $NiFe_2O_4$ sample had the smallest average pore size of 6 nm. In terms of magnetic properties, the cobalt ferrite sample had the highest saturation magnetization value. The replacement of Co with the other metals resulted in the decrease of the saturation magnetization value, and for nanocomposites their introduction into the hydroxyapatite structure also resulted in the decrease of the magnetic parameter values.

• The novel elements brought by this PhD thesis consisted in the use of two synthesized nanocomposites in two practical applications. The first application was about the study of the

absorption of Congo red dye on a $CoFe_2O_4$@HaP sorbent. Absorption tests yielded a dye absorption capacity of 27.97 mg/g, and sorbent reuse tests after three cycles resulted in an absorption capacity of 10.22 mg/g. The results obtained in this application were better than in other studies reported in the literature. Future research on this study would be to increase the adsorption capacity for the tested nanocomposite by improving its properties, and also to perform dye adsorption tests on the other synthesized samples. The second application was about testing the enzymatic activity of α-glucosidase upon interaction with $MgFe_2O_4$@HaP@APTES nanocomposite. Activity assays showed the preservation of α-glucosidase activity following nanocomposite coupling. The results obtained in this study will lead to the optimization of the enzyme activity and once achieved the use of the nanocomposite in applications for the identification of novel α-glucosidase inhibitors from natural extracts will be desired.

• Also in the framework of identifying applications involving the use of the synthesized compounds, the sorption capacity of ibuprofen on $CuFe_2O_4$ and $CuFe_2O_4$@HaP sorbents was tested. In order to verify whether the contact time between the ibuprofen solution and the sorbents influences the adsorption process, tests were carried out over a 24 h to 72 h interval. The maximum absorption percentages were obtained in the first 24 h and were 41.72% for $CuFe_2O_4$ and 53.83% for $CuFe_2O_4$@HaP. In the rest of the interval up to 72 h a plateau of absorption values was recorded. So the use of longer contact time does not produce changes in the adsorption process. However the sorbents used resulted in better results of the encapsulation efficiency of ibuprofen compared to the study taken as comparison term.

• For the series of mixed ferrites, silver coating was achieved by reducing it with glucose. The perspectives of this study are to utilize silver coated mixed ferrites in medical imaging tests as potential contrast agents.

Selective bibliography

[6] Jadhav, VV, Shirsat, SD, Tumberphale, UB, Mane, RS (2020). Properties of ferrites. *Elsevier eBooks, Elsevier BV*, pp.35–50. doi:https://doi.org/10.1016/b978-0-12-819237-5.00003-1.

[21] Hassanzadeh-Tabrizi, SA, Norbakhsh, H., Pournajaf, R., Tayebi, M. (2021). Synthesis of mesoporous cobalt ferrite/hydroxyapatite core-shell nanocomposite for magnetic hyperthermia and drug release applications. *Ceramics International*, 47(13), pp.18167–18176. doi: https://doi.org/10.1016/j.ceramint.2021.03.135.

[39] Sharifi, I., Zamanian, A., Behnamghader A. (2016). Synthesis and characterization of $Fe_{0.6}Zn_{0.4}Fe_2O_4$ ferrite magnetic nanoclusters using simple thermal decomposition method. *Journal of Magnetism and Magnetic Materials*, 412, pp.107–113. doi:https://doi.org/10.1016/j.jmmm.2016.03.091.

[87] Asadi, R., Abdollahi, H., Gharabaghi, M., Boroumand, Z. (2020). Effective removal of Zn (II) ions from aqueous solution by the magnetic $MnFe_2O_4$ and $CoFe_2O_4$ spinel ferrite nanoparticles with focuses on synthesis, characterization, adsorption, and desorption. *Advanced Powder Technology*, 31(4), pp.1480–1489. two:https://doi.org/10.1016/j.apt.2020.01.028.

[125] Gherca, D., Pui, A., Nica, V., Caltun, O., Cornei, N. (2014). Eco-environmental synthesis and characterization of nanophase powders of Co, Mg, Mn and Ni ferrites. *Ceramics International*, 40(7), pp.9599–9607. doi:https://doi.org/10.1016/j.ceramint.2014.02.036.

[126] Pui, A., Gherca, D., Carja, G. (2011). Characterization and magnetic properties of capped $CoFe_2O_4$ nanoparticles ferrites prepared in carboxymethylcellulose solution. *Digest Journal of Nanomaterials and Biostructures*, 6(4), pp.1783–1791.

[127] Kivrak, N., Taş, AC (2005). Synthesis of Calcium Hydroxyapatite-Tricalcium Phosphate (HA-TCP) Composite Bioceramic Powders and Their Sintering Behavior. *Journal of the American Ceramic Society*, 81(9), pp.2245–2252. doi: https://doi.org/10.1111/j.1151-2916.1998.tb02618.x.

[128] Arsad, MSM, Lee, PM, Hung, LK (2011). Synthesis and Characterization of Hydroxyapatite Nanoparticles and β-TCP Particles. *2nd International Conference on Biotechnology and Food Science, IPCBEE*, 7, pp.184–188.

[132] Hargreaves, JSJ (2016). Some considerations related to the use of the Scherrer equation in powder X-ray diffraction as applied to heterogeneous catalysts. *Catalysis, Structure & Reactivity*, 2(1-4), pp.33–37. doi: https://doi.org/10.1080/2055074x.2016.1252548.

[152] Rao, R., Huang, Y., Ling, Q., Hu, C., Dong, X., Xiang, J., Zhou, Q., Fang, S., Hu, Y., Zhang, Y., Tang, Q. (2023). A facile pyrolysis synthesis of Ni doped Ce_2O_3@CeO_2/CN composites for adsorption removal of Congo red: Activation of carbon nitride structure. *Separation and Purification Technology*, 305, p.122505. doi: https://doi.org/10.1016/j.seppur.2022.122505.

[153] Cordova Estrada, AK, Cordova Lozano, F., Lara Díaz, RA (2021). Thermodynamics and Kinetic Studies for the Adsorption Process of Methyl Orange by Magnetic Activated Carbons. *Air, Soil and Water Research*, 14, p.117862212110133. doi:https://doi.org/10.1177/11786221211013336.

[154] Pehlivan, M., Simsek, S., Ozbek, S., Ozbek, B. (2020). An optimization study on adsorption of Reactive Blue 19 dye from aqueous solutions by extremely effective and reusable novel magnetic nanoadsorbent. *DESALINATION AND WATER TREATMENT*, 191, pp.438–451. doi:https://doi.org/10.5004/dwt.2020.25753

[155] Peng, Q., Yu, F., Huang, B., Huang, Y. (2017). Carbon-containing bone hydroxyapatite obtained from tuna fish bone with high adsorption performance for Congo red. *RSC Advances*, 7(43), pp.26968–26973. doi: https://doi.org/10.1039/c6ra27055g.

[156] Nguyen, LM, Nguyen, NTT, Nguyen, TTT, Nguyen, DH, Nguyen, DTC. Tran, TV (2022). Facile synthesis of $CoFe_2O_4$@MIL–53(Al) nanocomposite for fast dye removal: Adsorption models, optimization and recyclability. *Environmental Research*, 215, p.114269. doi: https://doi.org/10.1016/j.envres.2022.114269.

[158] Dănilă, R.-Ș., Dumitru, I., Ignat, M., Pui, A. (2023). $CoFe_2O_4$@HaP as Magnetic Heterostructures for Sustainable Wastewater Treatment. *Materials*, 16(7), p.2594. doi: https://doi.org/10.3390/ma16072594.

[167] Wahab, A., Khan, GM, Muhammad, M., Khan, NR and Hussain, A. (2011). Pre-formulation investigation and in vitro evaluation of directly compressed ibuprofen-ethocel oral controlled release matrix tablets: A kinetic approach. *African Journal of Pharmacy and Pharmacology*, 5(19). doi: https://doi.org/10.5897/ajpp11.128.

[168] Anwar, N., Khan, A., Shah, M., Walsh, JJ, Anwar, Z. (2021a). Hybridization of Gold Nanoparticles with Poly(ethylene glycol) Methacrylate and Their Biomedical Applications. *Russian Journal of Physical Chemistry A*, 95(13), pp.2619–2631. doi:https://doi.org/10.1134/s0036024421130033.

[169] Anwar, N., Wahid, J., Uddin, J., Khan, A., Shah, M., Shah, SA, Subhan, F., Khan, MA, Ali, K., Rauf, M., Arif, M. (2021b). Phytosynthesis of poly (ethylene glycol) methacrylate-hybridized gold nanoparticles from C. tuberculata: their structural characterization and potential for in vitro growth in banana. *In Vitro Cellular & Developmental Biology - Plant*, 57(2), pp.248–260. doi: https://doi.org/10.1007/s11627-020-10150-4.

[170] Hussain, M., Rehan, T., Goh, KW, Shah, SI, Khan, A., Ming, LC, Shah, N. (2022). Fabrication of a Double Core–Shell Particle-Based Magnetic Nanocomposite for Effective Adsorption-Controlled Release of Drugs. *Polymers*, 14(13), p.2681. doi: https://doi.org/10.3390/polym14132681.

[171] Hussain, M., Rehan, T., Ul-Islam, M., Shehzad, O., Khan, A., Ullah, MW, Baig, A., Yang, G., Shah, N. (2023). Poly(2-acrylamido-2-methylpropane sulfonic acid)@butyl methacrylate latex anchored into polyethylene glycol diacrylate-based hydrogel composite for drug loading and controlled release studies. *Advanced Composites and Hybrid Materials*, 6(2). doi: https://doi.org/10.1007/s42114-022-00600-5.

[172] Md Rasib, SZ, Md Akil, H., Khan, A., Abdul Hamid, ZA (2019). Controlled release studies through chitosan-based hydrogel synthesized at different polymerization stages. *International Journal of Biological Macromolecules*, 128, pp. 531–536. doi: https://doi.org/10.1016/j.ijbiomac.2019.01.190.

[174] Gao, Y., Zhou, Y., Chandrawati, R. (2019). Metal and Metal Oxide Nanoparticles to Enhance the Performance of Enzyme-Linked Immunosorbent Assay (ELISA). *ACS Applied Nano Materials*, 3(1), pp.1–21. doi: https://doi.org/10.1021/acsanm.9b02003.

[175] Meryam Sardar, RA (2015). Enzyme Immobilization: An Overview on Nanoparticles as Immobilization Matrix. *Biochemistry & Analytical Biochemistry*, 04(02). doi: https://doi.org/10.4172/2161-1009.1000178.

[176] Zhang, Y., Shi, S., Chen, X., Peng, M. (2014). Functionalized magnetic nanoparticles coupled with mass spectrometry for screening and identification of cyclooxygenase-1 inhibitors from natural products. *Journal of Chromatography B*, 960, pp.126–132. doi:https://doi.org/10.1016/j.jchromb.2014.04.032.

[177] Chi, M., Wang, H., Yan, Z., Cao, L., Gao, X., Qin, K. (2022). Magnetic Ligand Fishing Using Immobilized Cyclooxygenase-2 for Identification and Screening of Anticoronary Heart Disease Ligands From Choerospondias axillaris. *Frontiers in nutrition*, 8. doi:https://doi.org/10.3389/fnut.2021.794193.

[178] Wubshet, SG, Brighente, IMC, Moaddel, R., Staerk, D. (2015). Magnetic Ligand Fishing as a Targeting Tool for HPLC-HRMS-SPE-NMR: α-Glucosidase Inhibitory Ligands and Alkylresorcinol Glycosides from Eugenia catharinae. *Journal of Natural Products*, 78(11), pp.2657–2665. doi:https://doi.org/10.1021/acs.jnatprod.5b00603.

[188] Karade, VC, Sharma, A., Dhavale, RP, Dhavale, RP, Shingte, SR, Patil, PS, Kim, JH, Zahn, DRT, Chougale, AD, Salvan, G. and Patil, PB (2021). APTES monolayer coverage on self-assembled magnetic nanospheres for controlled release of anticancer drug Nintedanib. *Scientific Reports*, 11(1). doi: https://doi.org/10.1038/s41598-021-84770-0.

[190] Cheng, G., Xing, J., Pi, Z., Liu, S., Liu, Z., Song, F. (2019). α-Glucosidase immobilization on functionalized Fe_3O_4 magnetic nanoparticles for screening of enzyme inhibitors. *Chinese Chemical Letters*, 30(3), pp.656–659. doi: https://doi.org/10.1016/j.cclet.2018.12.003.

[191] Shen, Y., Wang, M., Zhou, J., Chen, Y., Wu, M., Yang, Z., Yang, C., Xia, G., Tam, JP, Zhou, C., Yang , H., Jia, X. (2020). Construction of Fe_3O_4@α-glucosidase magnetic nanoparticles for ligand fishing of α-glucosidase inhibitors from a natural tonic Epimedii Folium. *International Journal of Biological Macromolecules*, 165, pp. 1361–1372. doi: https://doi.org/10.1016/j.ijbiomac.2020.10.018.

[192] Gherca, D., Ciocarlan, R., Cozma, D., Cornei, N., Nica, V., Influence of surfactant concentration (carboxymethylcellulose) on morphology and particle sizes of cobalt nanoferrites, *Chemistry Journal*, 64 (8) (2013) 3–6.

[193] Yasuda, M., Wilson, DR, Fugmann, SD, Moaddel, R. (2011). Synthesis and Characterization of SIRT6 Protein Coated Magnetic Beads: Identification of a Novel Inhibitor of SIRT6 Deacetylase from Medicinal Plant Extracts. *Analytical Chemistry*, 83(19), pp. 7400–7407. doi: https://doi.org/10.1021/ac201403y.

[196] Dănilă, R-Ș., Amarandi, RM., Ignat, M., Pui, A. (2023). Mesoporous $MgFe_2O_4$@HaP@APTES nanocomposite as scaffold for α-glucosidase coupling. *Materials today communications*, 36, pp.106427–106427. doi: https://doi.org/10.1016/j.mtcomm.2023.106427.

[197] Wei, K., Wang, Y., Lai, C., Ning, C., Wu, D., Wu, G., Zhao, N., Chen, X., Ye, J. (2005). Synthesis and characterization of hydroxyapatite nanobelts and nanoparticles. *Materials Letters*, 59(2-3), pp.220–225. doi:https://doi.org/10.1016/j.matlet.2004.08.034.

[201] Nlebedim, IC, Ranvah, N., Melikhov, Y., Williams, PI, Snyder, JE, Moses, AJ, Jiles, DC, (2009). Magnetic and magnetomechanical properties of $CoAl_xFe_{2-x}O_4$ for stress sensor and actuator applications, *IEEE Trans. Magn*. 45 (10), 4120–4123.

[202] Aoopngan, C., Nonkumwong, J., Phumying, S., Promjantuek, W., Maensiri, S., Noisa, P., Pinitsoontorn, S., Ananta, S., Srisombat, L. (2019). Amine-Functionalized and Hydroxyl-Functionalized Magnesium Ferrite Nanoparticles for Congo Red Adsorption. *ACS Applied Nano Materials*, 2(8), pp.5329–5341. doi: https://doi.org/10.1021/acsanm.9b01305.

[203] Sun, Y., Kunc, F., Balhara, V., Coleman, B., Kodra, O., Raza, M., Chen, M., Brinkmann, A., Lopinski, GP and Johnston, LJ (2019) . Quantification of amine functional groups on silica nanoparticles: a multi-method approach. Nanoscale Advances, 1(4), pp.1598–1607. doi: https://doi.org/10.1039/C9NA00016J.

[204] Ben Ali, M., El Maalam, K., El Moussaoui, H., Mounkachi, O., Hamedoun, M., Masrour, R., Hlil, EK, Benyoussef, A. (2016). Effect of zinc concentration on the structural and magnetic properties of mixed Co–Zn ferrites nanoparticles synthesized by sol/gel method. *Journal of Magnetism and Magnetic Materials*, 398, pp.20–25. doi: https://doi.org/10.1016/j.jmmm.2015.08.097.

[205] Andhare, DD, Patade, SR, Kounsalye, JS, Jadhav, KM (2020). Effect of Zn doping on structural, magnetic and optical properties of cobalt ferrite nanoparticles synthesized via. Co-precipitation method. *Physica B: Condensed Matter*, 583, p.412051. doi: https://doi.org/10.1016/j.physb.2020.412051.

[206] Kumar, S., Kumar, P., Singh, V., Kumar Mandal, U., Kumar Kotnala, R. (2015). Synthesis, characterization and magnetic properties of monodisperse Ni, Zn-ferrite nanocrystals. *Journal of Magnetism and Magnetic Materials*, 379, pp.50–57. doi: https://doi.org/10.1016/j.jmmm.2014.12.006.

[207] Iglesias-Silva, E., Rivas, J., León Isidro, LM, López-Quintela, MA (2007). Synthesis of silver-coated magnetite nanoparticles. *Journal of Non-Crystalline Solids*, 353(8-10), pp.829–831. doi: https://doi.org/10.1016/j.jnoncrysol.2006.12.050.

[208] Eka Putri, G., Rahayu Gusti, F., Novita Sary, A., Zainul, R. (2019). Synthesis of silver nanoparticles used chemical reduction method by glucose as reducing agent. *Journal of Physics: Conference Series*, 1317, p.012027. doi: https://doi.org/10.1088/1742-6596/1317/1/012.

[209] Ebrahimi, N., Rasoul-Amini, S., Ebrahiminezhad, A., Ghasemi, Y., Gholami, A., Seradj, H. (2016). Comparative Study on Characteristics and Cytotoxicity of Bifunctional Magnetic-Silver Nanostructures: Synthesized Using Three Different Reducing Agents. *Acta metallurgica Sinica. English letters/Acta Metallurgica Sinica*, 29(4), pp.326–334. doi:https://doi.org/10.1007/s40195-016-0399-9.

Papers published in Web of Science cited journals with impact factor

1) **Dănilă, R.-Ș.,** Dumitru, I., Ignat, Pui, A. (2023). $CoFe_2O_4$@HaP as Magnetic Heterostructures for Sustainable Wastewater Treatment. *Materials*, 16(7), p.2594. doi: https://doi.org/10.3390/ma16072594. **Impact factor 3.4**; Yellow zone (Q2);
2) **Dănilă**, R.-Ș., Amarandi, R.-M., Ignat, M., Pui, A. (2023). Mesoporous $MgFe_2O_4$@HaP@APTES nanocomposite as scaffold for α-glucosidase coupling. *Materials today communications*, 36, pp.106427–106427. doi:https://doi.org/10.1016/j.mtcomm.2023.106427., **Impact factor 3.8**; Yellow zone (Q2).

Cumulative Total Impact Factor = 3.4 + 3.8 = 7.2